GSAOI
CONCEPTUAL DESIGN REVIEW DOCUMENTATION

VOL. 1

Submitted to the International Gemini Project Office
under
AURA Contract No. 9414257-GEM00304

Research School of Astronomy and Astrophysics
Australian National University
Canberra, Australia

August 20-21, 2002

This page is left blank intentionally.

Executive Summary

The Gemini South Adaptive Optics Imager (GSAOI) will be the workhorse instrument used with Gemini's Multi-Conjugate Adaptive Optics (MCAO) system. The Research School of Astronomy and Astrophysics (RSAA) of the Australian National University (ANU) was selected to perform one of two Conceptual Design Studies for the instrument. The RSAA GSAOI Conceptual Design Study contract was signed in April 2002. This document presents the results of that study.

GSAOI is a diffraction-limited imaging instrument. It will use a single imaging scale of 0.02″/pixel and have a square field-of-view ~ 85″ on a side. GSAOI will be equipped with broad-band *Z*, *J*, *H*, *Ks*, and *K* filters and narrow-band zero-redshift emission-line filters.

Superb image quality is paramount. GSAOI will generate an RMS wave-front error of 46 nm, less than the MCAO allocation of 65 nm for its science instrument. This will deliver an instrumental Strehl ratio of > 94%. GSAOI will also have the ability to record defocused images that will be used to measure accumulated static wave-front errors through the entire optical system to the imager detector. The MCAO deformable mirror will be configured to null these wave-front errors. A fast cold shutter will allow the MCAO system to pause exposures in periods of poor adaptive-optics correction or when the MCAO lasers must be shut down due to the proximity of aircraft or satellites. An On-Detector Guide Window will be used to monitor image translation during exposures directly on the imager detector. A near-infrared On-Instrument Wave-Front Sensor (OIWFS) will track flexure variations between MCAO and GSAOI, monitor focus variations at the same wavelength as the science observation, and act as a tip-tilt reference for MCAO when required.

High sensitivity is essential to achieve the demanding science goals that have been set for the instrument. GSAOI will use efficient refractive optics to deliver the highest practical imager throughput. A pupil-viewing system will aid in realising high sensitivity by allowing the internal cold stop to be accurately aligned with the MCAO exit pupil.

Excellent astrometric performance is a high priority. The GSAOI optics have very low distortion so that the asymmetric MCAO distortion profile is not degraded or further complicated by GSAOI.

RSAA is well placed to design, construct, and commission GSAOI. It has recent experience in designing and constructing a diffraction-limited, near-infrared, adaptive-optics instrument for Gemini. The Near-infrared Integral-Field Spectrograph (NIFS) will be used with the ALTAIR facility adaptive-optics system on Gemini North. Many of the design issues that were addressed for NIFS are also relevant to GSAOI. These include issues associated with the wave-front error budget such as surface figure and alignment tolerances.

The wide field and high spatial resolution of MCAO require a larger near-infrared detector than has been available previously. The 4080×4080 pixel HAWAII-2RG detector mosaic that will be used in GSAOI is unprecedented. The focal-plane assembly will be designed and manufactured by GL Scientific, and the design will be tested by Don Hall. RSAA has recent experience working closely with GL Scientific in the design and manufacture of the focal-plane assembly for its Wide Field Imager 8k×8k CCD mosaic camera. Significant development will be required to optimize the performance of the state-of-the-art GSAOI detector system. RSAA is well placed to perform this task having recently developed the 2048×2048 HAWAII-2 detector system for NIFS.

MCAO is to be available at Gemini South on a short timescale. Consequently, a major design driver is to reuse as many existing instrument designs as possible in order to commission GSAOI on Gemini South ahead of the MCAO availability. This has necessitated reusing the Near-Infrared Imager (NIRI) cryostat

design, integration frame design, mechanism encoding system, temperature control system, Instrument Sequencer and Components Controller software, and OIWFS detector system.

RSAA pioneered this approach with great success in fast-tracking the design and construction of NIFS. RSAA has already assembled and tested NIFS duplicates of the NIRI cryostat, integration frame, mechanisms encoding system, temperature control system, Instrument Sequencer and Component Controller software. Delivery of the NIFS duplicate OIWFS detector system from the University of Hawaii is imminent. The RSAA workshops stand ready to duplicate these designs again, now that NIFS is moving into its assembly and commissioning phases.

The RSAA Director has declared that upon delivery of NIFS to Gemini North, GSAOI will assume the highest priority of all RSAA instrument developments.

RSAA will bring new resources to the project with AUSPACE, a Canberra-based aerospace company, assisting with the design and construction of the OIWFS. Prime Optics, in Queensland, designed the NIFS camera optics and have been involved in developing the GSAOI optical design. They will continue in this role.

Following the NIFS fast-tracked philosophy, it is proposed that the construction of duplicate components will begin immediately and will not be subject to further review. The GSAOI Preliminary Design Review is scheduled for 15-APR-03. It is proposed that this review will address only the imager and OIWFS optical designs and the design of the imager detector control system, as well as their interfaces to other subsystems and the extent to which they satisfy system requirements. The GSAOI Critical Design Review is scheduled for 30-SEP-03, with shipment to Gemini South planned for between 10-MAR-06 and 25-AUG-06, depending on contingencies.

This Conceptual Design Review Documentation consists of four volumes. Volume 1 contains a description of the science drivers for the instrument and the results of instrument modeling. Volume 2 contains a Technical Review of the proposed instrument. Volume 3 has three sections; a Management Plan for the further design, fabrication, and commissioning of the instrument, the Operational Concept Definition Document for the instrument, and the Functional and Performance Requirements Document for the instrument. Volume 4 contains a confidential costing for the further design, fabrication, and commissioning of GSAOI by RSAA.

SCIENCE REVIEW

GSAOI
Conceptual Design Review Document

Research School of Astronomy and Astrophysics
Australian National University
Canberra, Australia

August 20-21, 2002

This page is left blank intentionally.

Table of Contents

This page is left blank intentionally.

List of Acronyms

2MASS	Two Micron All Sky Survey
A&G	Acquisition and Guiding
ACS	Advanced Camera for Surveys
ADC	Atmospheric Dispersion Corrector
AGB	Asymptotic Giant Branch
ALTAIR	ALTitude-conjugated Adaptive optics for InfraRed
ANU	Australian National University
AO	Adaptive Optics
CDM	Cold Dark Matter
CFHT	Canada-France-Hawaii Telescope
CMD	Color-Magnitude Diagram
dE	Dwarf Elliptical
DSS	Digitized Sky Survey
FOV	Field-of-View
FPRD	Functional and Performance Requirements Document
FWHM	Full Width at Half Maximum
GSAOI	Gemini South Adaptive Optics Imager
HAWAII	HgCdTe Astronomical Wide Area Infrared Imager
HST	Hubble Space Telescope
ICM	Intra-Cluster Medium
IMF	Initial Mass Function
IOC	Input-Output Controller
ISS	Instrument Support Structure
ISAAC	Infrared Spectrometer And Array Camera
LGS	Laser Guide Star
LMC	Large Magellanic Cloud
MBE	Molecular Beam Epitaxy
MCAO	Multi-Conjugate Adaptive Optics
NASA	National Aeronautics and Space Administration
NDR	Non Destructive Read
NED	NASA Extragalactic Database
NGC	New General Catalog
NGS	Natural Guide Star
NGST	Next Generation Space Telescope
NICMOS	Near-Infrared Camera and Multi-Object Spectrograph
NIFS	Near-infrared Integral Field Spectrograph
NIRI	Near-InfraRed Imager
ODGW	On-Detector Guide Window
OIWFS	On-Instrument Wavefront Sensor
PACE	Producible Alternative to CdTe for Epitaxy
PDR	Preliminary Design Review
PNe	Planetary Nebulae
PSF	Point Spread Function
RMS	Root Mean Square
RSAA	Research School of Astronomy and Astrophysics
SALSA	Safe Aircraft Localization and Satellite Acquisition
SBF	Surface Brightness Fluctuations
SMC	Small Magellanic Cloud
SN	Supernova
USNO	United States Naval Observatory
VLT	Very Large Telescope

WFPC2	Wide Field and Planetary Camera 2
WFPC3	Wide Field and Planetary Camera 3
WWW	World Wide Web

1 Overview

1.1 Project History

The Research School of Astronomy and Astrophysics (RSAA) of the Australian National University (ANU) proposed in September 2001 to perform a Conceptual Design Study for the Gemini South Adaptive Optics Imager (GSAOI). Two groups were selected in November 2001 to do the studies. The Conceptual Design Study contract was signed with RSAA in April 2002. This Overview summarizes the contents of Volume 1 of the GSAOI Conceptual Design Review Documentation.

1.2 Scientific Context

High spatial resolution ground-based imaging is rightly the province of 8-10 m class optical/infrared telescopes. The Multi-Conjugate Adaptive Optics (MCAO) system on Gemini South will routinely deliver high Strehl ratio images over the full 2′ diameter Adaptive Optics (AO) field of the telescope with a uniform point spread function (PSF) and useful sky coverage. This unique facility opens new scientific domains. Many MCAO science programs will require direct imaging observations of faint targets, and many of these imaging observations will rely on high precision astrometry to achieve their goals. GSAOI will be the workhorse instrument that satisfies these MCAO imaging needs.

1.3 Top-Level Instrument Requirements

The top-level instrument requirements derive from the capabilities of the MCAO system and the characteristics of available near-infrared detectors (§2.2). They are summarized below:

- GSAOI shall operate between the 0.9 μm cut-on of the MCAO beam splitter and 2.4 μm where thermal emission dominates.
- GSAOI shall Nyquist sample diffraction-limited MCAO images at 1.65 μm by using a single image scale of 0.02″/pixel.
- GSAOI shall use a 4080×4080 pixel mosaic of Rockwell HAWAII-2RG HgCdTe/CdZnTe MBE detectors to record a square field-of-view 85″ on a side.
- GSAOI shall generate a root mean squared (RMS) wave front error of < 65 nm.
- A means shall be provided for measuring non-common-path wave-front errors at the GSAOI imager detector so that these errors can be nulled using the MCAO DM0 deformable mirror.
- GSAOI shall contain a comprehensive suite of broad-band and narrow-band filters.
- GSAOI shall have high throughput and low noise so that it reaches the deepest possible limiting magnitude.
- GSAOI shall have a uniform PSF across its field-of-view.
- GSAOI shall have stable image distortion that is either small or quantifiable.
- GSAOI shall have an internal fast shutter for pausing exposures under MCAO command.
- GSAOI shall include optics for viewing its internal cold stop.
- Ghost images generated by the GSAOI optics shall be at a level below 10^{-5} of the parent image.
- GSAOI shall have an On-Instrument Wave-Front Sensor (OIWFS) that will operate in any one of the *Z*, *J*, *H*, or *K* bands.
- The GSAOI OIWFS shall have a scale of 0.065″/pixel.
- GSAOI shall acquire OIWFS guide stars over the maximum practical field-of-view.
- The development of GSAOI shall be fast tracked by avoiding high-risk components and reusing existing designs wherever possible.

1.4 Science Drivers

The key science drivers for GSAOI were identified at a Gemini community workshop at Santa Cruz in October 2000. These were detailed in the MCAO Preliminary Design Review (PDR) documentation. Other projects have been added that are of prime interest to the Australian GSAOI science team members (§2.4). GSAOI will address the following diverse list of science drivers that extends from studies of nearby low mass stars to studies of distant forming galaxies:

- Low mass stellar and substellar mass functions in young star-forming regions such as the Orion Nebula Cluster.
- Stellar population variations in star-forming regions such as Ophiuchus, Corona Australis, and Chamaeleon.
- Open cluster mass functions to the bottom of the H-burning sequence and the end of the white dwarf cooling sequence to provide independent age determinations.
- Mass functions in nearby globular clusters over a range of metallicities.
- Stellar populations of super-star cluster analogs in the Galaxy and Magellanic Clouds such as NGC 3603 and 30 Doradus.
- Missing mass in Magellanic Cloud planetary nebulae.
- SN1a zero point calibration via red giant branch tip star distances to E/S0 galaxies.
- Proper motions of Local Group galaxies.
- Stellar populations in dwarf galaxies.
- Stellar populations in starburst regions of nearby galaxies.
- Evolution of dwarf irregular versus elliptical galaxies in different environments.
- Early chemical histories of nearby galaxy spheroids.
- Intergalactic stars in nearby galaxy clusters.
- Color distributions among extragalactic globular clusters.
- Measuring H_0 out to 60 Mpc using red supergiants.
- Measuring the bulk motion of galaxies to $cz < 6000$ km s^{-1} with surface brightness fluctuations.
- Spatially resolved spectral energy distributions of high redshift field galaxies.
- Evolution of galaxies in clusters.
- The formation of the disks of disk galaxies.
- Exploring dark energy via high redshift supernovae.

A common characteristic of these programs is that they require extremely deep near-infrared photometric imaging of extended regions. This necessitates high system throughput, excellent image quality, and a uniform PSF over the available field.

1.5 Instrument Simulations

1.5.1 Imager Performance Predictions

Limiting magnitudes have been modeled for a total on-source integration time of 1 hr in 0.4″ seeing through a 0.08″×0.08″ square aperture (§3.1.3.1). The results are listed in Table 1. These limiting magnitudes are not as deep as originally suggested for an idealized MCAO imager (MCAO PDR). The impact of the more realistic estimates on the science drivers is considered in §2.

Saturation magnitudes for a 5 s integration time and a detector full-well depth of 50,000 e are also listed in Table 1, as well as the Strehl ratio that was assumed for each filter and the sky brightness that resulted.

Table 1: Imager Sensitivities (10:1 in 1 hr)

Filter	Limiting Magnitude (mag)	Saturation Magnitude (mag)	Assumed Strehl Ratio	Sky Brightness (mag/arcsec^2)
Z	24.9	13.2	0.2	17.2
J	23.5	12.6	0.2	14.9
H	23.5	12.9	0.4	13.9
Ks	23.2	12.3	0.6	13.4
K	23.2	12.2	0.6	13.3
J continuum	22.4	10.2	0.2	15.0
H continuum	22.4	10.4	0.4	14.1
CH_4 (short)	23.0	11.9	0.4	13.9
CH_4 (long)	22.9	11.7	0.4	13.8
Ks continuum	22.2	9.9	0.6	13.8
Kl continuum	21.9	9.6	0.6	13.5
He I 1.0830 μm	22.9	10.3	0.2	16.0
H I Pγ	22.9	10.3	0.2	16.1
H I Pβ	21.8	10.1	0.2	13.9
[Fe II] 1.644 μm	22.1	10.3	0.6	13.7
H_2O	22.8	10.4	0.6	14.4
H_2 1-0 S(1)	22.0	9.9	0.6	13.4
H I Brγ	22.1	9.6	0.6	13.7
H_2 2-1 S(1)	22.0	9.7	0.6	13.5
CO 2-0 (bh)	21.8	9.6	0.6	13.3
CO 3-1 (bh)	21.6	9.5	0.6	13.0

1.5.2 Dominant Noise Sources

Background signals for each filter have been predicted for a integration time of 600 s (§3.1.3.2). These are listed in Table 2. Airglow emission dominates for all broad-band filters and most narrow-band filters. Thermal emission from the MCAO system makes a significant contribution in the two broad *K* bands and is dominant in the longer wavelength narrow-band filters. These background signals ensure that GSAOI will be background limited in all broad-band filters in integration times > 30 s and in all narrow-band filters in integration times > 150 s with a read noise of 10 e.

Table 2: Imager Background Contributions (600 s)

Filter	Airglow (e/pix)	Sky Thermal (e/pix)	Telescope Thermal (e/pix)	MCAO Thermal (e/pix)	Window Thermal (e/pix)	Total (e/pix)
Z	2152	0	0	0	0	2182
J	11182	0	0	0	0	11212
H	25130	1	4	13	1	25180
Ks	12822	236	1394	4289	276	19049
K	11007	554	2421	7448	483	21945
J continuum	1132	0	0	0	0	1162
H continuum	1873	0	0	0	0	1903
CH_4 (short)	8942	0	0	1	0	8973
CH_4 (long)	9465	0	2	5	0	9501
Ks continuum	1248	8	63	193	12	1554
Kl continuum	212	64	342	1053	68	1770
He I 1.0830 μm	423	0	0	0	0	453
H I Pγ	381	0	0	0	0	411
H I Pβ	2867	0	0	0	0	2897
[Fe II] 1.644 μm	2621	0	0	0	0	2652
H_2O	1032	40	39	121	8	1269
H_2 1-0 S(1)	1875	4	88	271	17	2285
H I Brγ	796	8	115	353	23	1325
H_2 2-1 S(1)	491	37	284	874	57	1774
CO 2-0 (bh)	65	90	414	1273	83	1954
CO 3-1 (bh)	66	139	531	1634	107	2507

1.5.3 Imager On-Detector Guide Window Performance

Limiting magnitudes for the imager On-Detector Guide Window (ODGW; §3.1.3.3) that achieve a RMS centroiding accuracy of 2 mas in integration times of 0.01 s (i.e., fast tip-tilt) and 30 s (i.e., slow flexure monitoring) are listed for each broad-band filter in Table 3.

Table 3: Imager ODGW Sensitivities (2 mas RMS)

Filter	Limiting Magnitude 10 ms integration (mag)	Limiting Magnitude 30 s integration (mag)
Z	13.9	22.0
J	13.1	21.2
H	12.7	20.5
Ks	12.0	19.8
K	11.9	19.7

1.5.4 OIWFS Performance

Limiting magnitudes for the OIWFS (§3.5.1) that achieve a RMS centroiding accuracy of 2 mas in integration times of 0.005 s (i.e., fast tip-tilt) and 30 s (i.e., slow flexure monitoring) are listed in Table 4.

Table 4: OIWFS Sensitivities (20:1 per image)

Filter	**Limiting Magnitude 5 ms integration (mag)**	**Limiting Magnitude 30 s integration (mag)**
Z	10.4	19.6
J	9.9	18.4
H	10.4	18.5
Ks	9.9	18.2
K	9.9	18.1
ZJ	11.0	19.4
HK	11.1	18.9

1.5.5 Guide Star Availability

The probability of finding at least one $K \leq 10$ mag guide star in a random MCAO science field is very low (< 0.1%; §3.5.2). Consequently, there will be limited scope for using the OIWFS or ODGW for fast tip-tilt monitoring. The probability of finding at least one $K \leq 18$ mag guide star somewhere in the MCAO field is high (99.9% at b = 30º, 88.9% at b =60º, and 80.3% at b = 90º). This will permit slow flexure and focus monitoring in most science fields.

2 Science Drivers

2.1 Scientific Context

The Gemini MCAO system will be the facility AO system for Gemini South. It will routinely provide uniform, diffraction-limited image quality at near-infrared wavelengths across an extended field-of-view. Useful levels of atmospheric turbulence compensation will be achieved over the full 2′ diameter AO field-of-view, the maximum possible with the Gemini telescope design. Sky coverage will also be comparable or somewhat superior to ALTAIR, the facility AO system on Gemini North. MCAO will use three deformable mirrors conjugated to different altitudes in the atmosphere. These will be driven with commands computed from wave-front sensor measurements of five laser guide stars (LGSs) and three natural guide stars (NGSs). The system will be able to operate with fewer than three natural guide stars, but with reduced performance.

Many of the science programs that will be undertaken with MCAO require direct imaging of extremely faint extragalactic objects.

A goal for MCAO is to perform high precision astrometry. The narrow AO-corrected PSF will permit accurate relative positional measurements. It is unclear at present whether MCAO can deliver the high image-scale stability needed to perform high accuracy absolute astrometry. If this proves possible, MCAO will be a unique astrometric instrument that will be capable of measuring proper motions for many Galactic objects on relatively short timescales.

2.2 Top Level Instrument Requirements

MCAO will deliver mean Strehl ratios in median seeing at the zenith of ~ 0.20 at *J*, ~ 0.40 at *H*, and ~ 0.60 at *K*. These will decline to ~ 0.05 at *J*, ~ 0.18 at *H*, and ~ 0.39 at *K* at a zenith distance of 45°. Consequently, GSAOI will be most competitive at near-infrared wavelengths between the 0.9 μm cut-on of the MCAO beam splitter and 2.4 μm where thermal emission dominates.

The diffraction limit of Gemini South is 0.032″ at *J*, 0.042″ at *H*, and 0.057″ at *K.* A compromise image scale is required for a fixed-format camera. The higher Strehl ratios achieved at longer near-infrared wavelengths should bias this compromise. So too should the larger fields-of-view realized by Nyquist sampling only at the longer wavelengths. Under-sampling short wavelength PSFs is a concern, but one that ultimately must be tolerated. Consequently, GSAOI will use a single image scale of 0.02″/pixel.

All MCAO imaging programs require the largest possible field-of-view. Since MCAO will provide at least partial image correction over the full 2′ diameter AO field of the telescope, the GSAOI field-of-view is driven by available detector real-estate. The largest available near-infrared detector is the Rockwell HAWAII-2RG HgCdTe/CdZnTe Molecular Beam Epitaxy (MBE) detector with a 2040×2040 array of 18 μm pixels. GSAOI will use a mosaic of four HAWAII-2RG detectors arranged in a 2×2 grid. The HAWAII-2RG detectors are mounted in a three-side buttable package so each detector will be separated by < 2.5 mm. The resulting square field-of-view will be 85″ on a side.

The MCAO wave-front error budget allocates a RMS wave-front error of 65 nm to the science instrument. This corresponds to a Strehl ratio of 0.941 at 1.65 μm. GSAOI must meet this demanding specification.

Static non-common-path wave-front errors due to the Instrument Support Structure (ISS) science fold mirror and the GSAOI optics will be reduced by sensing the wave-front shape at the GSAOI imager detector and configuring the MCAO DM0 deformable mirror to null these errors.

GSAOI should contain a comprehensive suite of broad-band and narrow-band filters suffient to address all MCAO imaging requirements. It should have high throughput and low noise so that imaging observations reach as deep a limiting magnitude as possible. The image quality should be uniform over the full field-of-view to permit accurate photometry. Image distortion should be stable and either small or quantifiable at a level that permits astrometric observations.

GSAOI should contain an internal fast shutter that will allow the MCAO system to pause exposures in periods of poor AO correction or when the MCAO Safe Aircraft Localization and Satellite Acquisition (SALSA) system triggers a laser shutdown due to the proximity of an aircraft or satellite to the science beam.

Achieving the deepest possible limiting magnitude involves maximizing the instrumental throughput and minimizing background emission. Pupil-viewing optics will be essential for aligning the internal cold stop with the MCAO exit pupil. Reducing ghost images to acceptable levels is also important because each science field must contain up to three MCAO natural guide stars that may be bright. In general, ghost images should be at a level of below 10^{-5} of the parent image.

An OIWFS is required to 1) monitor slow flexure variations between MCAO and GSAOI, 2) monitor slow variations in the altitude of the atmospheric sodium layer that are manifest as slow focus variations in the MCAO output beam, and 3) sense fast tip-tilt and focus variations when the OIWFS is used as one of the three MCAO natural guide star wave-front sensors. The OIWFS will monitor these variations at the wavelength of the science observation in order to avoid chromatic effects. Modeling presented in §3.4 indicates that an OIWFS image scale of 0.065″/pixel is required to optimally centroid the AO-corrected MCAO image.

Guide star availability is a critical parameter dictating the scientific scope of MCAO and hence GSAOI. Simulations presented at the MCAO PDR suggest that natural guide stars with limiting magnitudes of 19.6, 19.5, and 19.2 will be needed in dark, grey, and bright skies, respectively. The three MCAO natural guide stars must be widely spaced. It was estimated at the MCAO PDR that suitable combinations of 19.5 magnitude natural guide stars would be found over 77% of the sky at a Galactic latitude of 30° and over 18.5% of the sky at the Galactic pole. Sky coverage variations with sky brightness are not dramatic.

All GSAOI observations will require a suitable OIWFS guide star to at least monitor slow tip-tilt and focus variations. Maximizing the OIWFS sky coverage is therefore an essential component of maximizing the science scope of GSAOI.

GSAOI is required in the period 2005-2006 when the MCAO system will be commissioned on Gemini South (MCAO PDR). This short timescale requires that the design and manufacture of GSAOI must be fast tracked. GSAOI should contain the minimum of high-risk components, with none requiring extensive new development. GSAOI should reuse existing instrument designs wherever possible.

A complete list of the instrument requirements is presented in the Functional and Performance Requirements Document (FPRD, Vol. 3).

2.3 Summary of Instrument Parameters

The GSAOI instrumental parameters that satisfy the top-level instrument requirements are summarized below:

- Wavelength range: 0.9-2.4 μm.
- Pixel size: 0.02″×0.02″ on sky.
- Broad-band filters: *Z*, *J*, *H*, *Ks*, *K*.
- Narrow-band filters: zero-redshift emission lines.
- Detector: Rockwell 4080×4080 HAWAII-2RG HgCdTe/CdZnTe MBE, 18 μm pixels.
- Fast cold shutter: Command driven from MCAO.
- Pupil viewer: Inserted without disturbing imager optics.
- Near-infrared On-Instrument Wave-Front Sensor:

- Wavelength range: 0.9-2.4 μm.
- Steerable over 120″ FOV.
- Image scale: 0.065″/pixel.
- Filters: *Z*, *J*, *H*, *Ks*, *K*, *ZJ*, *HK*.
- Instantaneous field-of-view: 0.5″ diameter.

2.4 Science Team Members

The Australian GSAOI science team consists of astronomers from three Australian institutions. All are keen to use GSAOI to advance their personal research interests. The team members are:

Michael Bessell (Australian National University)
Gary Da Costa (Australian National University)
Michael Dopita (Australian National University)
Paul Francis (Australian National University)
Kenneth Freeman (Australian National University)
Brad Gibson (Swinburne University of Technology)
Helmut Jerjen (Australian National University)
Peter McGregor (Australian National University)
Bruce Peterson (Australian National University)
Brian Schmidt (Australian National University)
Christopher Tinney (Anglo-Australian Observatory)
Peter Wood (Australian National University)

2.5 Overview of Science Drivers

GSAOI will be the workhorse instrument for Gemini's MCAO system. The key science drivers for GSAOI were identified at a Gemini community workshop at Santa Cruz in October 2000. These were detailed in the MCAO PDR documentation. The science cases that have been elaborated include:

- Low mass stellar and substellar mass functions in young star-forming regions such as the Orion Nebula Cluster.
- Stellar population variations in star-forming regions such as Ophiuchus, Corona Australis, and Chamaeleon.
- Open cluster mass functions to the bottom of the H-burning sequence and the end of the white dwarf cooling sequence to provide independent age determinations.
- Mass functions in nearby globular clusters over a range of metallicities.
- Stellar populations of super-star cluster analogs in the Galaxy and Magellanic Clouds such as NGC 3603 and 30 Doradus.
- SN1a zero point calibration via red giant branch tip star distances to E/S0 galaxies.
- Stellar populations in starburst regions of nearby galaxies.
- Evolution of dwarf irregular versus elliptical galaxies in different environments.
- Early chemical histories of nearby galaxy spheroids.
- Intergalactic stars in nearby galaxy clusters.
- Color distributions among extragalactic globular clusters.
- Spatially resolved spectral energy distributions of high redshift field galaxies.
- Evolution of galaxies in clusters.

It is of key importance to determine whether these science cases can be achieved with the proposed GSAOI instrument and, if not, what more restricted observations are possible. Both limiting sensitivity and guide star availability must be considered in making this assessment.

We add the following science cases to the above list. These projects are of prime interest to Australian GSAOI science team members:

- Missing mass in Magellanic Cloud planetary nebulae.
- Proper motions of Local Group galaxies.
- Stellar populations in dwarf galaxies.
- Measuring H_0 out to 60 Mpc using red supergiants.
- Measuring the bulk motion of galaxies to $cz < 6000$ km s^{-1} with surface brightness fluctuations.
- The formation of the disks of disk galaxies.
- Exploring dark energy via high redshift supernovae.

For each of these cases we now describe the science goal, and then ask the following questions:

- Is the science goal achievable within the sensitivity limits of the proposed instrument?
- Are MCAO guide stars available?
- Does the observation place special requirements on the instrument design?

2.6 The Orion Nebula - A Detailed Study of a Nearby Massive Star-Forming Region

2.6.1 Science Goal

This project was proposed in the MCAO Science Case (RPT-AO-G0107). Deep imaging at *J*, *H*, and *K* is required to identify all stellar objects, brown dwarfs, and planetary mass objects in the central region of the Orion Nebula Cluster down to ~ 1 M_J (Jupiter mass). This is required to establish the initial mass function (IMF) in a region of intense massive star formation. A detailed knowledge of the stellar and substellar IMF is fundamental to understanding fragmentation processes in molecular clouds, determining the nature of starburst galaxies, and describing the chemical evolution of the Universe.

The potential for high quality astrometry with MCAO provides a new means of identifying contaminating foreground stars. The Orion Nebula Cluster proper motion is predominantly along the line of sight, so large transverse motions may indicate contaminating sources (0.5 mas yr^{-1} for a transverse velocity of 1 km s^{-1} at the distance of the Orion Nebula). Background stars remain a problem and in fact Lucas et al. (2001) have shown that some J = 17-18 mag background stars are seen through the molecular cloud. This problem will increase towards J = 23 mag, so the interpretation of color-magnitude diagrams obtained towards Orion will critically depend on assigning accurate membership probabilities.

Accurate membership probabilities can be assigned even for a system with low proper motion like Orion to H ~ 21 mag over a 2 yr period (250 μas in 4 hr per epoch). This corresponds to masses down to ~ 3-5 M_J, and represents a significant improvement in the robust assignment of cluster membership over what is currently possible through spectroscopy at the H ~ 17-18 mag level. Proper motion information will permit a very robust determination of the Orion Nebula Cluster mass function down to well below the ~ 10 M_J deuterium-burning limit. This mass range overlaps with mass function measurements for extra-solar planets already being obtained from radial velocity work.

2.6.2 Sensitivity Limit

Photometry to J ~ 26 mag and H and K ~ 25 mag over a 6×6 arcmin field was original proposed in order to reach 1 M_J objects in the Orion Nebula Cluster. The revised limiting magnitude (H ~ 23.5, 10:1 in 1 hr) is more restrictive. However, it will still be possible to detect 2 M_J objects with ages of ~ 2×10^6 yr in the cluster in 4 hr exposures and to confidently assign membership probabilities to 3-5 M_J objects. This can be seen from Figure 1 where H magnitudes based on the models of Baraffe et al. (2002) are plotted for planets and brown dwarfs of different masses and ages of 1 Myr and 5 Myr.

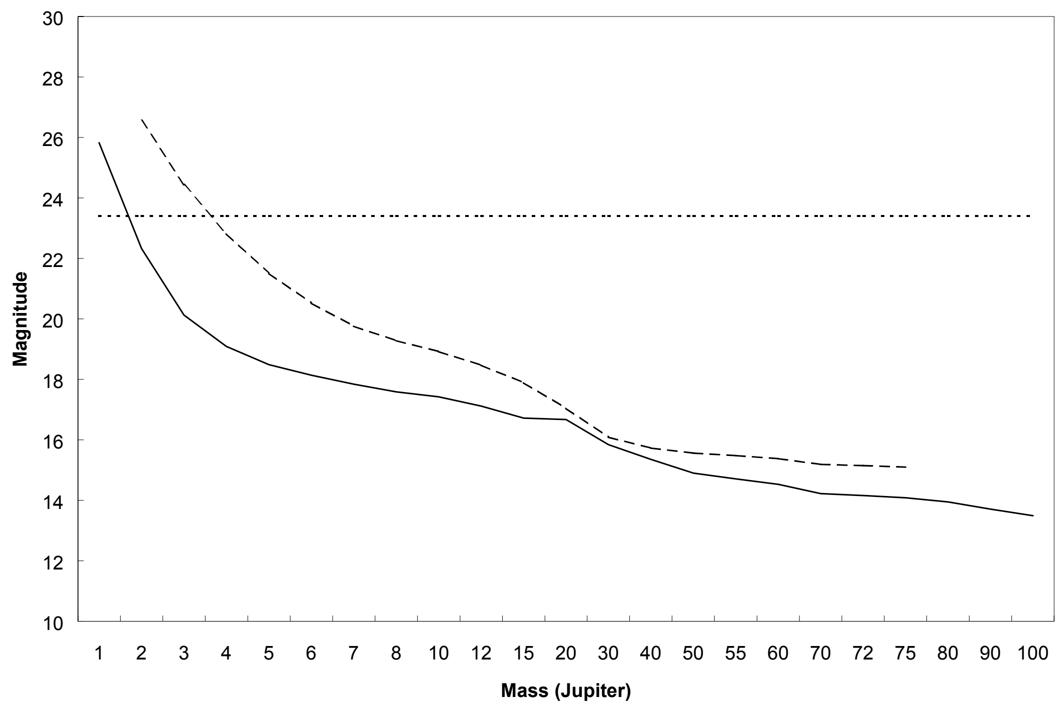

Figure 1: *H* magnitudes of 1 Myr old (*solid curve*) and 5 Myr old (*dashed curve*) planets and brown dwarfs of different masses from Baraffe et al. (2002). The horizontal line corresponds to the 10:1 in 1 hr limit.

2.6.3 Guide Star Availability

There is no difficulty finding suitable guide stars in the center of the Orion Nebula Cluster, as shown in Figure 2. This figure shows Digitized Sky Survey (DSS), 2MASS, WFPC2, and NICMOS images centered on θ^1C Ori (the DSS image is saturated by nebula emission). The fields of the four GSAOI detectors are overlaid, along with the outline of the 2′ diameter MCAO field and the track of the five MCAO LGSs. Three MCAO NGSs are marked by triangles. A small circle marks the OIWFS star.

The bright nebular background and the bright Trapezium stars limit the sensitivity for detecting faint point sources in the central region. Figure 3 shows a region 3′ east of θ^1C Ori. There are no WFPC2 or NICMOS images of this field and the DSS image remains saturated, so no US Naval Observatory (USNO) stars are cataloged. The 2MASS near-infrared image suggests that suitable guide stars exist. However, other material will have to be consulted to confirm these selections.

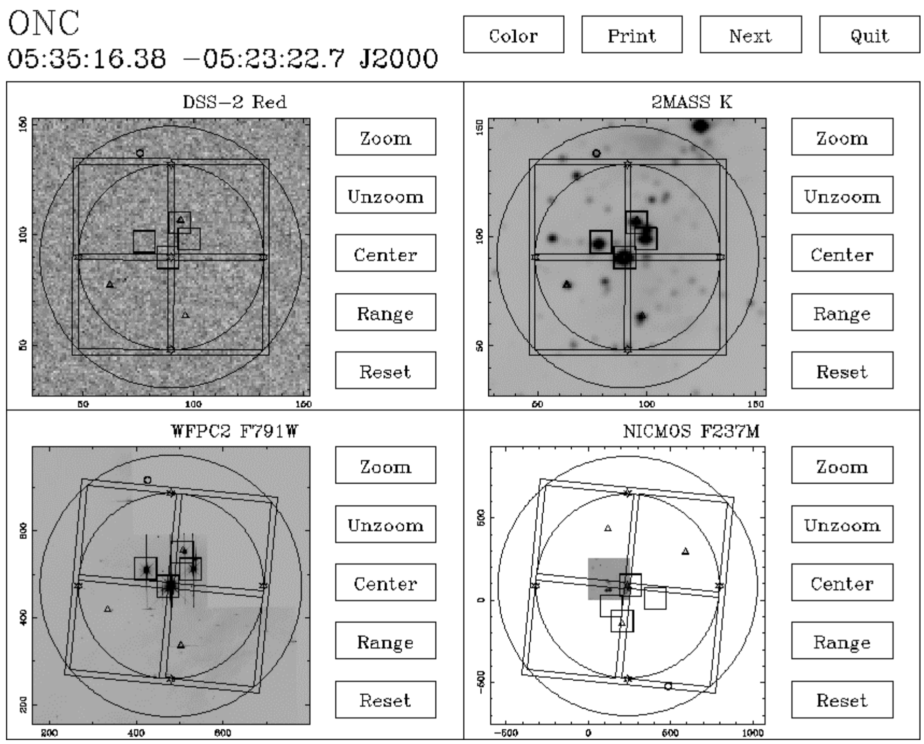

Figure 2: DSS, 2MASS, WFPC2, and NICMOS images of the Orion Nebula Cluster central region. Small squares mark USNO catalog stars. The four GSAOI detectors and the first fold mirror are indicated by large squares. The large outer circle delimits the MCAO field. Stars mark the five LGSs. Small triangles mark the three NGSs. A small circle marks the OIWFS guide star.

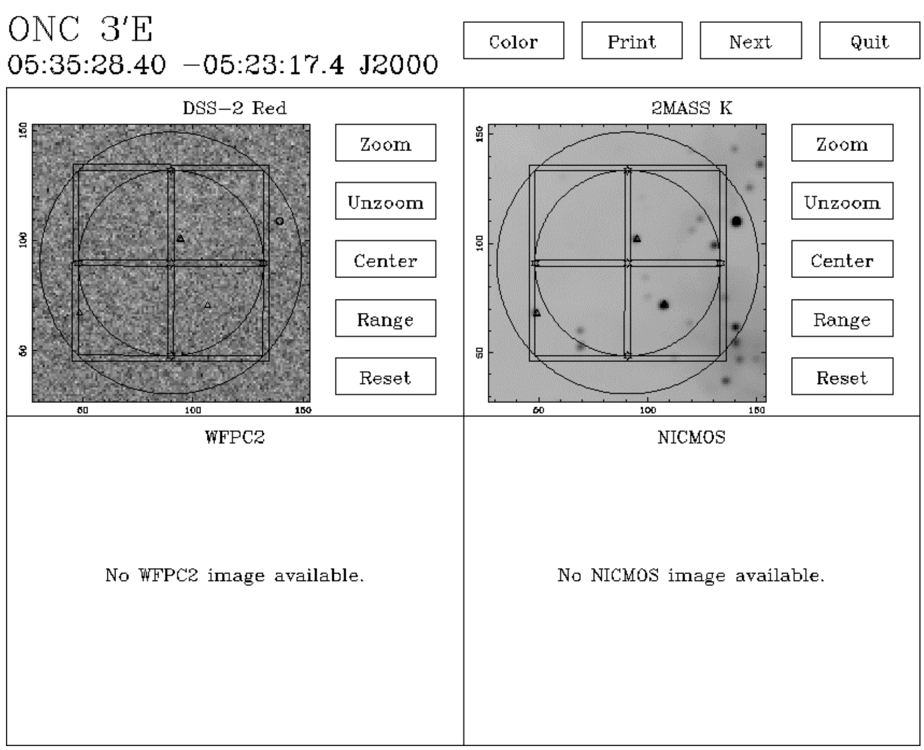

Figure 3: DSS and 2MASS images of a region 3′ east of the Orion Nebula Cluster.

2.6.4 Special Requirements

The main requirement of this project is to detect faint unresolved objects in the vicinities of multiple bright stars. Low ghost image intensities and low scattered light levels in the imager will be essential.

Long-term high astrometric precision is also essential. The critical issue is whether the astrometric distortion is repeatable at a level significantly below the targeted precision of ~ 250 μas per epoch, for likely changes of the instrument due to flexure and temperature variations. Astrometric distortion residuals of ~ 50 μas per epoch may be required to achieve this.

A simple and straightforward way to calibrate distortion is by imaging a matrix mask at the first telescope focal plane in the MCAO system. Failing that, an acceptable result might be achieved by imaging the 5×5 grid of the MCAO NGS source simulator. The focus mask in the GSAOI focal plane wheel will contain an array of pinholes that will at least allow distortion within the imager to be calibrated.

2.7 Young Stellar Super-Clusters

2.7.1 Science Goal

This project was proposed in the MCAO Science Case (RPT-AO-G0107). It requires deep *J*, *H*, and *K* imaging of Galactic and Magellanic Cloud analogs of the super star clusters identified in starburst galaxies. Super star clusters dominate the star formation in starburst galaxies, and have almost certainly been involved in the star formation history of the Galaxy. Understanding the stellar populations in these massive star-forming regions, and in particular the interplay between high- and low-mass star formation, is a key goal of this project. Mass functions ranging from the massive O-type stars to objects below the hydrogen-burning limit will be studied in nearby young super star clusters such as NGC 3603 in the Galaxy and 30 Dor in the Large Magellanic Cloud (LMC). Measurements in narrow-band filters (such as CO and Brγ) will give information on the stellar populations.

2.7.2 Sensitivity Limit

NGC 3603 has been measured in 0.4″ seeing down to $J \sim 21$ mag with ISAAC on the VLT (Brandl et al. 1999). These observations sampled down to masses of ~ 0.1 $M_{\rm Sun}$ (~ 100 M_J), assuming an age of ~ 1 Myr. Extending this a further 2.5 mag to the estimated GSAOI *J* limit (~ 23.5 mag 10:1 in 1 hr), or below, will reach substellar objects with masses < 13 M_J.

Images of similar depth in the 30 Dor region will reach pre-main sequence stars with masses of a few ×0.1 $M_{\rm Sun}$ assuming an age of ~ 1 Myr.

2.7.3 Guide Star Availability

NGC 3603 fits easily within the GSAOI field-of-view (Figure 4). There appears to be an abundance of MCAO NGSs, although the lack of USNO catalog stars leaves their brightness uncertain. The lack of a 2MASS image complicates the selection of an OIWFS guide star.

The region of the 30 Dor cluster is shown in Figure 5. There appears to be no problem identifying suitable guide stars. However, their brightness cannot be determined from the USNO catalog because the DSS images are saturated.

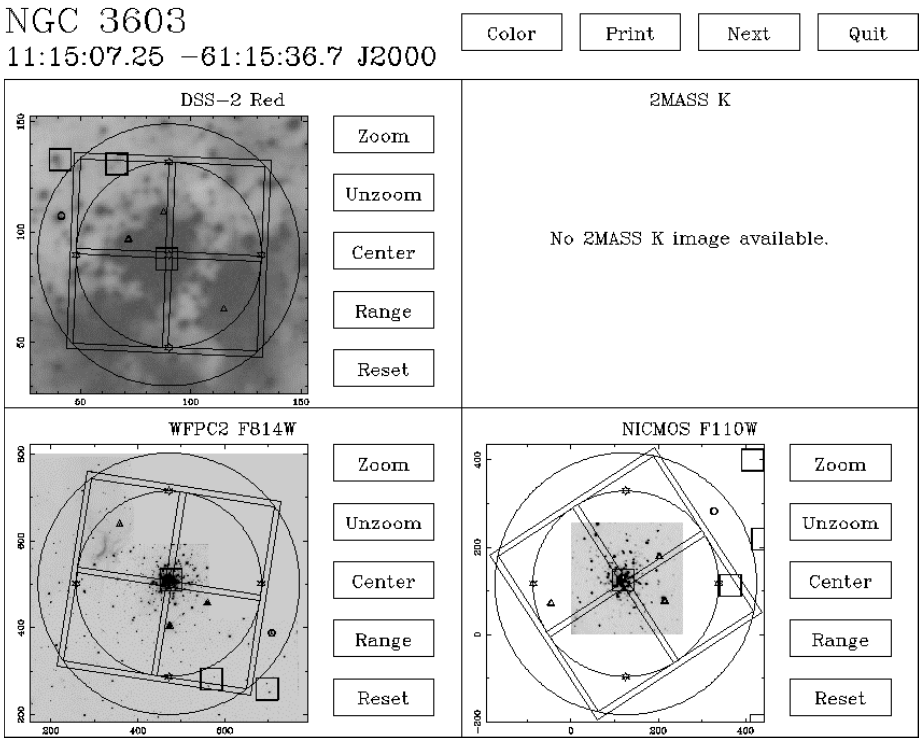

Figure 4: DSS, WFPC2, and NICMOS images of the NGC 3603 star cluster.

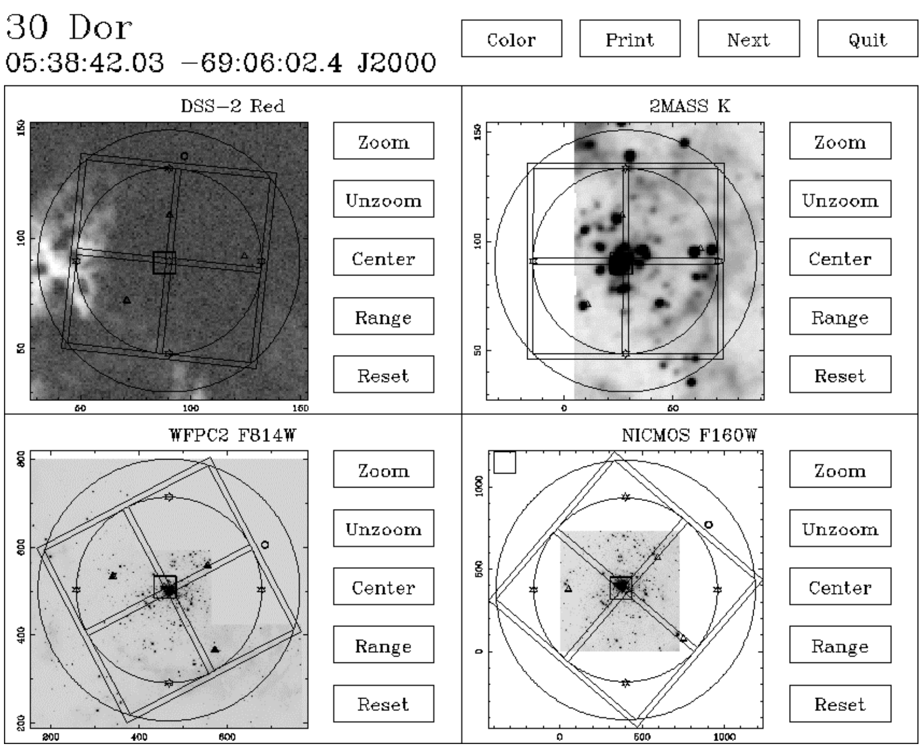

Figure 5: DSS, 2MASS, WFPC2, and NICMOS images of the 30 Dor star cluster.

2.7.4 Special Requirements

The main requirements for this project are high Strehl ratio to reduce crowding, a stable and uniform PSF over the field to permit accurate photometry, and low ghost image intensity to permit high dynamic range measurements in the vicinities of bright stars. A large field-of-view is required, but also good sampling of the PSF at all wavelengths.

2.8 White Dwarf Cooling Ages in Galactic Open Clusters

2.8.1 Science Goal

This project was proposed in the MCAO Science Case (RPT-AO-G0107). The goal is to detect the termination of the white dwarf cooling sequence in nearby open star clusters, and hence derive cluster ages that are independent of the normal main sequence turnoff method. The cooling sequence ends at intrinsically faint magnitudes even for young clusters and contamination by stellar and extragalactic interlopers has always been a concern. The potential for accurate proper motion measurements with GSAOI offers a means of overcoming this difficulty. Proper motion measurements will be especially useful for distinguishing white dwarfs from distant star-forming blue galaxies.

A large area must be mosaiced in order to ensure that the cluster white dwarf luminosity function is adequately sampled.

2.8.2 Sensitivity Limit

Six nearby open clusters spanning a range of ages were identified in the MCAO Science Case; NGC 6405, NGC 2516, NGC 3532, NGC 3680, NGC 6253, and Coll 261. The white dwarf sequence termination has been detected in the 570 Myr old open cluster NGC 2099 at M_V = 11.95±0.3 mag (Kalirai et al. 2001), as expected from its main sequence turnoff age and white dwarf cooling models. This suggests that the white dwarf termination should be detectable with GSAOI in the first four of the clusters listed, with the termination at $H \sim 23.4$ mag in the oldest of these, NGC 3680. Termination magnitudes in the older clusters, NGC 6253 and Coll 261, are expected to be significantly below the GSAOI sensitivity limit of $H \sim 23.5$ mag (10:1 in 1 hr).

2.8.3 Guide Star Availability

There appears to be no shortage of guide stars towards these Galactic open clusters. The extreme central region of NGC 6405 is shown in Figure 6.

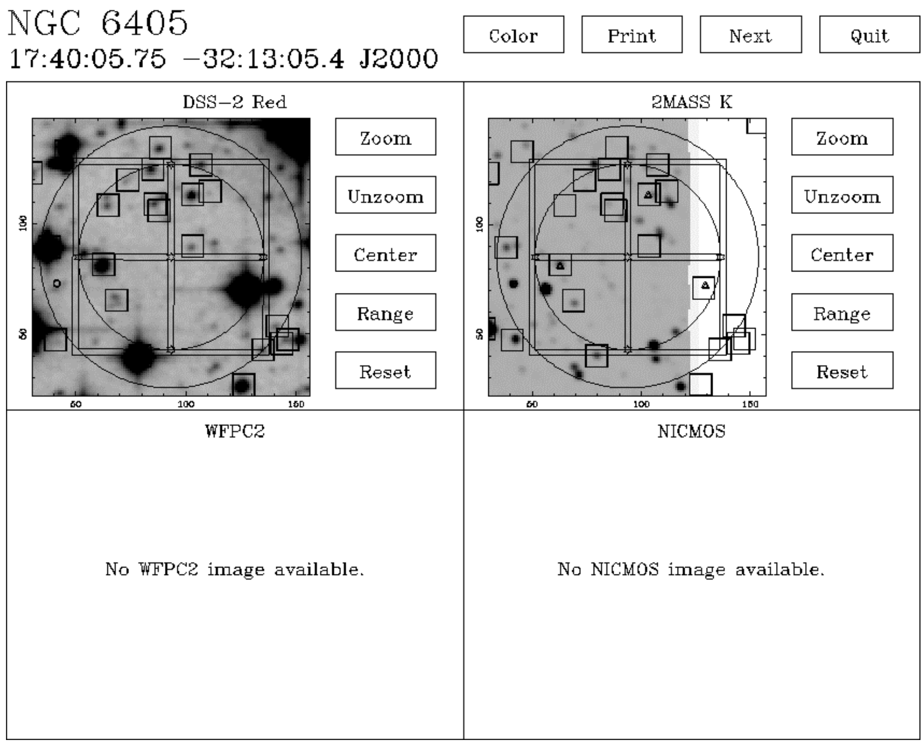

Figure 6: DSS and 2MASS images of the extreme central region of the open cluster NGC 6405.

2.8.4 Special Requirements

The main requirement for this project is high astrometric precision to identify open cluster members. The maximum possible field size with good PSF sampling is desirable to increase the number of detected stars. Stars are expected over a range of ~ 10 mag so high dynamic range is also desirable.

2.9 Globular Cluster Mass Functions Over a Range of Metallicities

2.9.1 Science Goal

This project was proposed in the MCAO Science Case (RPT-AO-G0107). It aims to probe the main sequence mass function and substellar limit in old metal-poor Galactic globular clusters. The mass limit of stars at the bottom of the hydrogen-burning main sequence is predicted to be metallicity dependent: this prediction will be tested. Deep *JHK* images reaching the end of the population-II main sequence are required for several globular clusters. Measurements of proper motions will be used to identify cluster members and remove field stars.

2.9.2 Sensitivity Limit

The MCAO Science Case lists five southern globular clusters that are suitable for this project; NGC 6553, NGC 104, NGC 6121, NGC 6752, and NGC 6397. The bottom of the hydrogen-burning main sequence in globular clusters should occur at $M_J \sim 13$ mag and $M_K \sim 11$ mag. Sixteen fields and at least two filters are required per cluster, so exposure times are effectively limited to ~ 1 hr. Given the expected GSAOI sensitivities ($J \sim 23.5$ mag and $K \sim 23.2$ mag 10:1 in 1 hr), it is likely that the bottom of the main sequence will be detectable in only NGC 6121 and NGC 6397, and detection at J will be difficult even in these clusters ($J \sim 24.7$ mag and $K \sim 22.7$ mag for NGC 6121; $J \sim 24.8$ mag and $K \sim 22.8$ mag for NGC 6397). The bottom of the main sequence is expected to be at $J > 26.0$ mag and $K > 24.0$ mag in the other clusters.

The revised GSAOI sensitivity limits severely impact the science potential of this project.

2.9.3 Guide Star Availability

There is no difficulty identifying guide stars, at least in the central regions of NGC 6121 and NGC 6397. The core of NGC 6121 is shown in Figure 7.

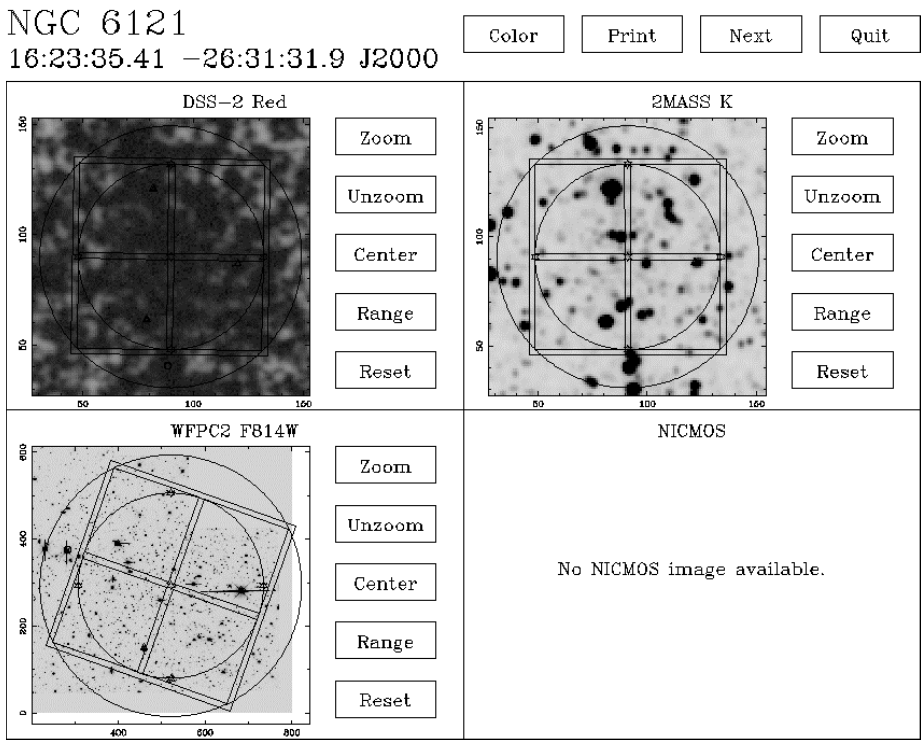

Figure 7: DSS, 2MASS, and WFPC2 imagers of the core of the globular cluster NGC 6121.

2.9.4 Special Requirements

A uniform PSF across the GSAOI field-of-view is required to perform accurate photometry at faint levels.

2.10 Missing Mass in Magellanic Cloud Planetary Nebulae

2.10.1 Science Goal

Despite vast increase in our understanding of the evolutionary nature of planetary nebulae (PNe) during the last three decades, a central question remains: *where is the missing mass?* Theoretical evolutionary tracks predict that all stars with masses in the range 1.4-8 M_{Sun} should become PNe. According to the models, much of the mass of these stars is lost during a series of thermal pulses in the asymptotic giant branch (AGB) phase of evolution. Observations reveal that the central star mass is close to 0.6 M_{Sun}, except for a few Peimbert Type I nebulae (e.g., NGC 6302 with 0.8 M_{Sun}, or a handful of objects in the LMC). However, the ionized nebular mass of the PN is typically of order 0.1 M_{Sun}, and the derived mass is found to depend very strongly on the radius of the nebula. Clearly, much of the mass of the planetary nebula shell must remain un-ionized, and much of it may be in molecular form. This molecular gas has been mapped in the 110.2 GHz (1-0) transition of ^{12}CO in a number of nearby PNe. These observations confirm the much greater extent of the nebula in molecular gas. In the infrared, the nebula can be mapped in the 2.122 μm 1-0 S(1) and 2.248 μm 2-1 S(1) lines of molecular hydrogen, which in most objects seem to be fluorescently excited by UV radiation from the central star. Generally speaking, the size of the observed nebula is larger, and the estimated molecular hydrogen masses much greater, than the ionized gas component. The nebula of NGC 7027 (Dayal et al. 2000) is a splendid example of this.

For Galactic objects, accurate mass inventories are bedeviled by uncertainties in the PN distance scale, which can only be resolved by the study of a population of PN at a known distance and having low field reddening. The Magellanic Cloud PNe are ideal for this. At optical wavelengths, the Hubble Space Telescope (HST) has been used to systematically investigate the morphologies and ionization of the ionized component. These data typically have a spatial resolution of a little better than 0.1″, which corresponds to a linear resolution of ~ 0.02 pc at the distance of the LMC. This is quite sufficient to reveal the internal morphology, given that the typical diameter of a PNe is about 0.1 pc and some objects are as large as 1.0 pc across including the faint outer structure.

With its superb spatial resolution, the GSAOI instrument will be ideally suited to perform a systematic study of both the PNe and the proto-planetary nebulae in the Magellanic Clouds at a spatial resolution that matches the observations that have been made by HST of the ionized gas components. The quality of the images that could be obtained would be comparable with the NICMOS images that HST has obtained of PNe towards the Galactic center. Not only can the extent and distribution of the molecular hydrogen be determined, but the PNe can also be mapped in the [Fe II] 1.644 μm line, which in some PNe reaches an intensity in excess of 2×10^{-14} erg cm^{-2} s^{-1} arcsec^{-1} (Welch et al. 1999) and which traces the positions of shocks driven into the molecular shell by the high pressure of the ionized zone and fast winds that have shaped the PNe morphology.

For the Magellanic Cloud PNe, these data will enable us to derive quantitative data that cast direct light on the evolution of PNe and on their AGB precursors. The positions of the central stars on the Hertzsprung-Russell diagram are known, we can distinguish between H-burning and He-burning stars, and the dynamical ages of the nebulae can be determined for these PNe.

2.10.2 Sensitivity Limit

The average intensity of [Fe II] 1.644 μm emission in the outer parts of the Galactic planetary nebula Hubble 12 is ~ 8×10^{-15} erg s^{-1} cm^{-2} arcsec^{-2} (Welch et al. 1999). The sensitivity limit for GSAOI in the [Fe II] 1.644 μm filter is expected to be ~ 4×10^{-15} erg s^{-1} cm^{-2} arcsec^{-2} (10:1 per resolution element in 1 hr). This is comfortably below the expected average intensity, so it will be possible to confidently detect any low surface brightness structure that is present.

2.10.3 Guide Star Availability

Twenty-six LMC PNe (Vassiliadis et al. 1998 and references therein) with HST data have been searched for suitable MCAO guide stars. Acceptable guide stars are probably available for all of these targets. We illustrate this with the example of LMC-SMP 2 in Figure 8. Nevertheless, it is apparent that the ability to dither the image to achieve accurate sky subtraction is often restricted by the need to have suitable guide stars at every dither position.

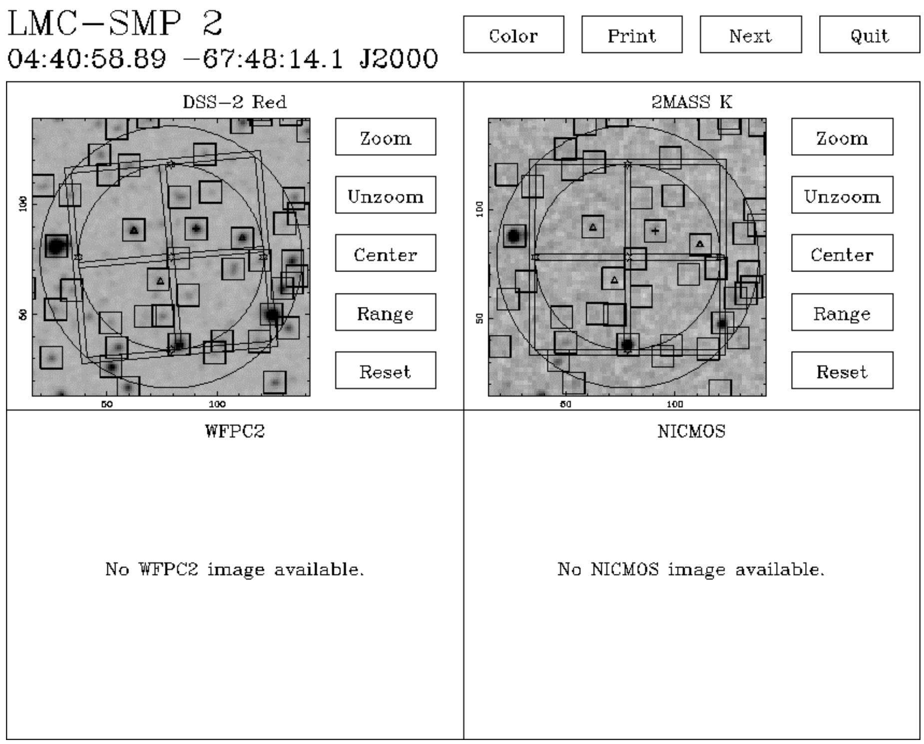

Figure 8: DSS and 2MASS images of the LMC planetary nebula LMC-SMP 2. A small cross identifies the target.

2.10.4 Special Requirements

The Large and Small Magellanic Clouds have heliocentric Doppler shifts of +260 and +150 km s^{-1}, respectively. The "zero redshift" narrow band emission line filters should be sufficiently wide (or have appropriately shifted central wavelengths) to ensure that emission lines from both Galactic and Magellanic Cloud objects are passed with good transmission.

A means of rapidly traversing the OWIFS guide field to acquire new guide stars will contribute significantly to the efficiency with which dithered observations are obtained.

A uniform PSF over the GSAOI field will permit deconvolution algorithms to be used to further improve spatial resolution.

2.11 Proper Motions of Local Group Galaxies

2.11.1 Science Goal

The accretion of satellites (Searle & Zinn 1978) has become recognized as being of fundamental importance to the formation and evolution of the Milky Way halo. This model was initially proposed because differences in the globular cluster populations in the inner and outer halo suggested the existence of an age spread (Zinn 1993; van den Bergh 1993). Studies in recent years have provided several lines of evidence to support the importance of the accretion scenario, including:

- Numerous examples of kinematic substructures along independent lines of sight that suggest the halo is threaded with "streams" of stars (e.g., Arnold & Gilmore 1992; Côté et al. 1993; Majewski et al. 1994).
- The discovery of the "smoking gun" of the Sagittarius dwarf spheroidal galaxy that has been "caught in the act" of being disrupted by the Milky Way (Ibata et al. 1994).

However, the properties of a typical accretor remain unclear.

It has been long suggested that the Milky Way satellites define a plane about the Galactic center (Kunkel & Demers 1976; Lynden-Bell 1976). More recently, two separate planes have been proposed (Majewski et al. 1994; Lynden-Bell & Lynden-Bell 1995). If such "mega-streams" are associated with a single accretion event, a typical accretor would have a mass comparable to the Magellanic Clouds. Alternatively, accretion events may have involved only single dwarf spheroidal-like satellites, implying a "maximally chaotic" outer halo in which a typical stream has a mass of $< 10^8\ M_{Sun}$, and the "mega-streams" are not dynamically significant. The distinction between high- and low-mass accretors is important. The latter (10^7-$10^8\ M_{Sun}$) will produce kinematically distinct streams that survive for long times in the halo, while negligibly heating the Galactic thin disk. The accretion of a massive satellite, however, would produce a kinematically indistinct cloud of stars and heat the disk to much larger scale heights than we see today.

Space velocities will allow us to determine how well mixed the outer halo really is, and test directly for the existence of the "mega-streams". Proper motions are vital for this, as they alone distinguish between chance alignments and true streams. Precise proper motions for the Galaxy's satellites are essential if we are to distinguish between these models.

Such data are also of fundamental importance to the determination of the gravitational potential of the Galaxy at large galactocentric radii, and to the measurement of the total mass of our Galaxy.

GSAOI offers the prospect of the precise measurement for many southern hemisphere satellite galaxies such as Fornax, Sculptor, Carina, Sextans, Phoenix, and others. Dedicated surveys have revealed the presence of unresolved quasars behind many of these target galaxies (Tinney et al. 1997; Tinney 1999), and similar surveys of the remaining targets will be straightforward to carry out. At the magnitudes of interest, both quasars *and* suitable giants in the galaxies for use as a "galaxy" reference frame are available (the technique is to measure the quasar's reflex motion relative to a frame of galaxy giants). At precisions of ~ 180 μas per epoch over 5 years, 1σ precisions for proper motion measurement of ~ 40 μas yr^{-1} become feasible, making the proper motions of all these galaxies detectable in a program totaling ~ 200-300 hr over 5 years.

2.11.2 Sensitivity Limit

The Sculptor, Sextans, Carina, Fornax, Phoenix dwarf spheroidal galaxies have distance moduli of 19.5, 19.7, 20.0, 20.7, and 23.2, respectively. The red giant branch tip occurs at $M_K \sim -6.5$ mag, so these stars will be detected at $K \sim 13.0$, 13.2, 13.5, 14.2, and 16.7 mag, respectively. These objects are easily measured with GSAOI. Integration times will be set by the required astrometric precision, rather than photometric precision.

2.11.3 Guide Star Availability

Guide star availability will depend on the positions of background quasars projected on the foreground galaxy. This is uncertain at present.

2.11.4 Special Requirements

Long-term high astrometric precision is essential.

2.12 Stellar Populations in Dwarf Galaxies

2.12.1 Science Goal

It is probably no exaggeration to claim that the most important outstanding question in the study of the formation and evolution of dwarf galaxies is the origin of the remarkable diversity of star formation histories observed among the dwarf Ellipticals (a class that includes the so-called dwarf Spheriodals) of the Local Group. Prior to the first hints of a discrepancy in the early 1980s, the paradigm that dEs galaxies consist entirely of old stars was universally accepted, and amongst those unfamiliar with developments in the field, this view is still surprisingly prevalent. Yet it is now abundantly clear that the simple picture of dEs as consisting of entirely old (age > 10 Gyr) stars is no longer valid. For example, among the Milky Way's dE companions we see systems with dominant old populations, systems with minor intermediate-age (age ~ 2 to 10 Gyr) components, and systems where the intermediate-age component dominates the old stars. Even in these latter systems there is further variety; in Carina the on-going star formation occurred in a number of discrete episodes while in Fornax it was approximately continuous. This variety of star formation histories is not restricted to the Galaxy's companions. Recent observations with HST/WFPC2 have shown that M31's dEs have also had extended epochs of star formation.

Despite the large amount of observational data available for Local Group dEs, there is currently no explanation for the diversity of star formation histories, only hints. For example, among the Galaxy's companions there is a tendency for the systems with stronger intermediate-age components to lie at larger Galactocentric distances. This also appears to be the case for M31's companions where, at least among the lower luminosity dE companions, it is the more distant system And II that has a definite intermediate-age population; systems closer to M31 lack such stars. These results suggest that proximity to a "parent galaxy" influences the evolution of dwarf galaxies. Indeed, recent theoretical simulations have shown how a dwarf irregular on an initial "plunging" orbit in the Milky Way halo can be converted into a dE satellite. At the same time it is notable that, with one exception, all the isolated dwarfs in the Local Group are not dEs; they show either recent or on-going star formation. The one local exception to this hypothesis that "parent galaxies" nurture initial gas-rich dwarf companions into dE galaxies, is the isolated dE Tucana. Despite its lack of association with any large galaxy, it nevertheless possesses a dominant old stellar population and there are no signs of any intermediate-age component. The existence of this system demonstrates that proximity to a large galaxy cannot be the only factor governing the evolution of dwarf galaxies.

To make progress in understanding the processes that govern dwarf galaxy evolution, we need to study systems beyond the Local Group. Such studies can be targeted at dEs that occupy a variety of environments, thereby allowing us to more readily distinguish between intrinsic properties and "parent galaxy" influence. In particular, we need to target a sizeable fraction of the dEs within our "Local Volume", the sphere of radius ~10 Mpc centered on the Local Group, seeking to establish what fraction of these systems show intermediate-age populations. This volume includes the relatively loose Sculptor Group, the more compact Cen A group, and a variety of other galaxy aggregations such as the loose association of galaxies that contain the Circinus galaxy at a distance of 6-7 Mpc. The observational signature of an intermediate-age population is the presence of upper-AGB stars, i.e., stars with sufficient mass to evolve on the AGB to luminosities above that of the red giant branch tip. For such stars there is a good correlation between the luminosity of the brightest upper-AGB star and the age of the intermediate-age component. The observations are best done at near-infrared wavelengths since these pass bands cover the wavelengths where the majority of the flux is emitted. Bolometric corrections are therefore small and well defined and the amplitude of variability is much reduced relative to the optical. Single epoch J and K band measurements then suffice for a determination of the bolometric magnitudes (two pass bands are required as the bolometric correction to the K magnitude is a function of J-K color). Although current near-infrared imagers can reach upper-AGB stars in the nearer of the dEs within the Local Volume using relatively long integration times, given the likelihood of a diversity of star formation histories, a sizeable sample of dwarfs in a variety of environments needs to be studied if underlying trends are to be revealed. GSAOI is the ideal instrument with which to carry out this program.

2.12.2 Sensitivity Limit

An 8-10 Gyr old upper-AGB star, the upper limit to what we might call an intermediate-age population, has a bolometric magnitude $M_{\mathrm{Bol}} \sim -4.1$ mag and $M_{\mathrm{K}} \sim -6.8$ mag with J–$K \sim 1.2$. We need to measure the bolometric magnitude to a precision of $\sim \pm 0.2$ mag, including both photometric and distance modulus uncertainties. This can be achieved if both the J and K magnitudes are measured to a signal-to-noise ratio of ~ 10. The expected GSAOI sensitivities are such that the upper-AGB component can be measured for any dE within the 10 Mpc sphere of the Local Volume in ~ 1 hr of on-source integration at K and 5 hr of integration at J. This is sufficient sensitivity to allow targeting of a well-defined sample of dEs covering a range of both intrinsic properties (surface brightness, total magnitude, length scale, etc.) and environmental parameters (distance from potential parent galaxy, parent galaxy type, local galaxy density, orbit timescales/crossing times, etc.).

2.12.3 Guide Star Availability

There are sufficient candidate dE galaxies within the Local Volume that restricting the sample to only those systems with appropriate guide stars is not likely to be a severe requirement. The relatively small size of the targets also allows some flexibility in the positioning, increasing the probability of acquiring a suitable set of guide stars. An example of the Centaurus A group dwarf elliptical ESO219-010 is show in Figure 9.

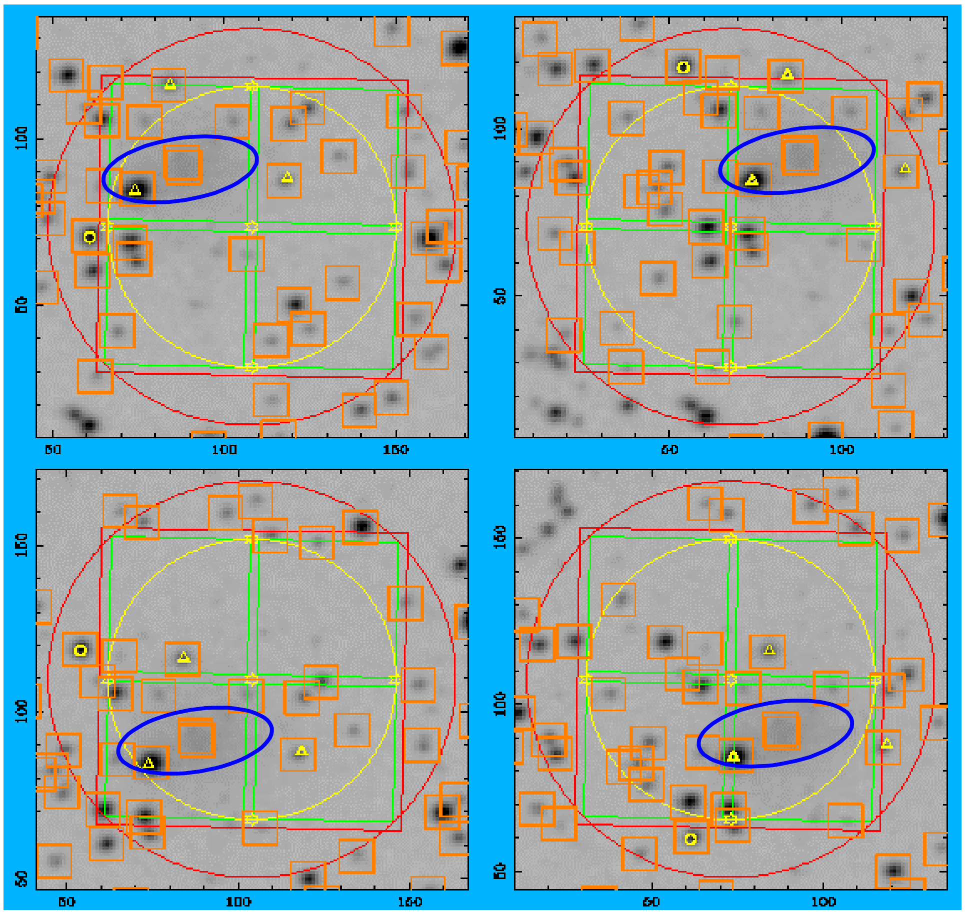

Figure 9: Dither pattern for an observation of the dwarf galaxy ESO219-010. The DSS-2 image of ESO219-010 is shown as a grayscale. The large ellipse indicates the object. The fields of the four GSAOI imager detectors are shown as squares. A large circle indicates the 2′ diameter MCAO field. A large square marks the outline of the GSAOI first fold mirror. The LGS constellation is shown as stars on a circle. The actual LGSs will appear somewhere on this circle depending on the time of observation. US Naval Observatory catalog stars are enclosed in boxes. The three NGS selected are marked by triangles. A small circle marks the OIWFS guide star.

2.12.4 Special Requirements

The program described here is essentially a routine application of the GSAOI and therefore does not impose any special requirements on the instrument other than a uniform PSF across the field to permit accurate photometry.

2.13 Calibration of the Supernovae Ia Zeropoint

2.13.1 Science Goal

This project was proposed in the MCAO Science Case (RPT-AO-G0107). The goal is to measure red giant branch tip distances to E/S0 galaxies containing supernovae (SNe) Ia. These SNe Ia can then be used to tighten the SNe Ia distance scale calibration. The red giant branch tip occurs at $M_J \sim -5.3$ mag and $M_K \sim -6.5$ mag, but it is necessary to reach somewhat below the tip in order to make a confident detection. The MCAO Science Case lists seven E/S0 galaxies with well measured SNe Ia; NGC 1316, NGC 5128, NGC 4374, NGC 1380, NGC 4526, NGC 5253, and NGC 5005.

2.13.2 Sensitivity Limit

The expected GSAOI sensitivity ($J \sim 23.5$ mag and $Ks \sim 23.2$ mag 10:1 in 1 hr) is such that the red giant branch tip is likely to be detectable only in NGC 5128 and NGC 5253 at $J \sim 22.5$ mag and $Ks \sim 21.3$ mag and $J \sim 22.9$ mag and $Ks \sim 21.7$ mag, respectively. The red giant branch tip has already been detected in NGC 5128 (Soria et al. 1996). The red giant branch tip occurs at $J \sim 25.1$ mag and $K \sim 23.9$ mag in NGC 5005 and at $J > 25.7$ mag and $K > 24.5$ mag in the other four galaxies. It is therefore likely that GSAOI will permit only a minor improvement in the SNe Ia distance scale calibration.

2.13.3 Guide Star Availability

Suitable guide stars appear to be available in a field ~ 1.5 arcmin SE of the nucleus of NGC 5253 (Figure 10). The MCAO NGSs have $R \sim 15.8$, 18.0, and 18.1 mag in the USNO catalog. Concerns about the calibration of the USNO catalog in the southern hemisphere dictate caution in choosing the two fainter stars. The OIWFS guide star has $R \sim 16.7$ mag, but the absence of a 2MASS image leaves its near-infrared brightness uncertain.

Guide stars are available in a field 4′ south of NGC 5128.

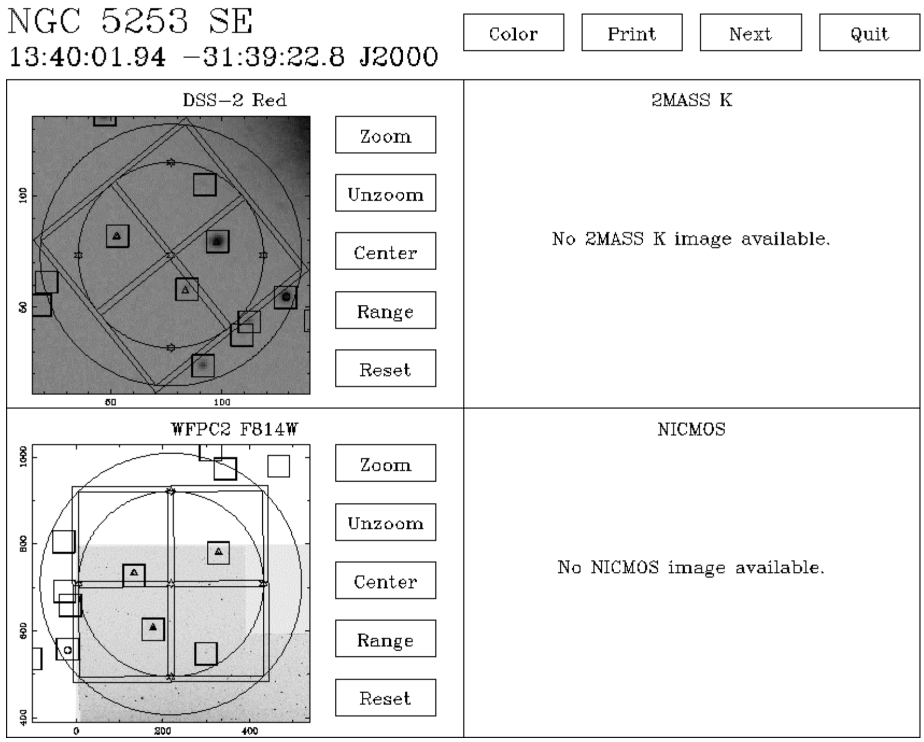

Figure 10: DSS and WFPC2 images of a field ~ 1.5 arcmin SE of NGC 5253.

2.13.4 Special Requirements

The project is essentially a routine application of the GSAOI and therefore does not impose any special requirements on the instrument other than a uniform PSF across the field to permit accurate photometry.

2.14 Intracluster Stars in Nearby Galaxy Clusters

2.14.1 Science Goal

This project was proposed in the MCAO Science Case (RPT-AO-G0107). Faint intracluster light is seen in some of the more distant galaxy clusters. It is currently believed to come from stars stripped from galaxies by the harassment process (fast encounters of galaxies leading to impulsive heating and then stripping by the tidal field of the cluster). This belief needs to be more firmly established.

In the nearer clusters, like Virgo and Fornax, observations of diffuse light are very difficult. Individual stars are much more useful tracers of the stellar intracluster medium (ICM) in nearby clusters; intracluster planetary nebulae have already been detected in the Virgo and Fornax clusters.

Galaxies of intermediate mass are believed on theoretical grounds to be the ones most affected by harassment. They can be transformed into loosely bound dwarfs, with much of their stellar mass lost into the ICM. The harassment process would produce a stellar ICM with substantial substructure in space and velocity. This can be tested directly, and some progress has been made in this direction using the planetary nebulae.

Red giants are much more abundant than planetary nebulae, and provide ideal probes of the ICM. In principle, one can use color-magnitude diagrams (CMDs) of the upper giant branch of the intracluster stellar population to derive the surface density distribution and the metallicity of the stellar ICM. This would allow us to quantify the spatial substructure of the ICM; also, using the metallicity-luminosity relation for galaxies, it would give useful observational constraints on the kinds of galaxies that have contributed most to the stellar ICM.

The observational goal is then to construct stellar CMDs in many locations of the Virgo and Fornax clusters; these are the nearest significant galaxy clusters, and are both known to contain a stellar ICM.

2.14.2 Sensitivity Limit

Here is the problem. To do anything useful on the stellar ICM, we need a CMD down to at least 1 mag below the tip of the red giant branch. The brightest red giants have M_J = -5.5, M_H = -6.2, and M_K = -6.5 mag. The distance modulus of the Virgo and Fornax clusters is ~ 31.0. So we need images with a signal-to-noise ratio of at least 5 at J = 26.5, H = 25.8, and K = 25.5 mag. This seems well out of reach for the GSAOI. Even with a small aperture of 4×4 pixels, the integration times at J, H, and K are about 60, 20, 20 hr, respectively.

2.15 Measuring H_0 Out to 60 Mpc Using Red Supergiants

2.15.1 Science Goal

Despite intense efforts using HST over the past decade, there is still fierce debate about the value of the Hubble Constant, although most people now agree that it has a value between 55 and 80 km s^{-1} Mpc^{-1}. The HST Key Project team has presented the most significant body of work (Freedman et al. 2001). They used Cepheid variables out to 20 Mpc as the calibrating method for a host of secondary distance indicators such as Type Ia supernovae, surface brightness fluctuations, and the Tully Fisher method. However, the small numbers of objects, difficulties in HST CCD calibrations, large extinction corrections, and the difficulty of combining surface brightness fluctuation distances to early-type galaxies with Cepheid distances to late type galaxies have all complicated this work. Luminous red supergiants provide a new method of measuring the Hubble constant that is independent of Cepheid distances. The red supergiant method offers high precision, ease of use, low vulnerability to extinction, and a single method that can be applied to the LMC, SMC, nearby galaxies, and other late-type galaxies out to 60 Mpc with GSAOI.

The brightest red supergiants pulsate with periods of 400 to 900 days and have M_K ~ -11 (Wood, Bessell, & Fox 1983). Typical full K band amplitudes are ~ 0.25 mag. These luminous red supergiants lie on a K-log P relation with scatter about the relation of ~ 0.25 mag. The LMC has roughly 20 of these variable red supergiants so that a galaxy of this relatively small size can give a distance modulus accurate to ~ 0.05 mag. Larger spiral galaxies will yield larger numbers of red supergiants and hence a more accurate distance modulus. Imaging in the K band maximizes the contrast between the red supergiants and the galaxy background. Red supergiants will be found by their variability, which distinguishes them from bright star clusters.

The degree of contrast of the red supergiants against the galaxy background is a relevant concern that will be more problematic at larger distances. If a typical background giant star has M_K ~ -5 mag, its apparent magnitude at a distance of ~ 60 Mpc is K ~ 28.9 mag. There are ~ 83 such giant stars per 0.06″×0.06″ resolution element in a region with a K band surface brightness of ~ 18.0 mag arcsec^{-2}. Background fluctuations due solely to statistical variations in the number of these stars will be at the level of ΔK ~ ±0.1 mag per resolution element. The addition of a single M_K = -11 mag red supergiant to this background will cause a fluctuation of -1.5 mag per resolution element. Consequently, it is very unlikely that surface brightness fluctuations due to variations in the number of background stars will impede measurement of the luminous red supergiants.

2.15.2 Sensitivity Limit

A signal-to-noise ratio of ~ 25 is required to detect variability. The GSAOI K band sensitivity is such that a M_K ~ -11 mag red supergiant can be detected with this signal-to-noise ratio at 60, 50, 40, 30, and 20 Mpc in 3.6, 1.7, 0.7, 0.2, and 0.04 hr. Approximately 12 such measurements spread over ~ 2 years at 2-3 month intervals are required to determine a pulsation period. At least three galaxies are required at each distance, so this project will require a total of ~ 250 hr of integration time to complete.

This program can be expanded easily to increase the number of galaxies surveyed, and improve the precision of Hubble constant measurement.

2.15.3 Guide Star Availability

There is a multitude of acceptable galaxies at distances < 60 Mpc, so it is convenient to choose only galaxies that have suitable guide stars.

2.15.4 Special Requirements

A uniform PSF is required over the GSAOI field to allow accurate measurement of stars across the entire galaxy.

2.16 Measuring the Bulk Motions of Galaxies to cz < 6000 km/s with Surface Brightness Fluctuations

2.16.1 Science Goal

It is widely accepted that the evolution of the large scale structure of the Universe is driven by dark matter. Understanding this dark matter continues to be one of Astronomy's great unsolved problems. Measuring the bulk motions of galaxies allows us to map the overall mass distribution of the Universe in a way that is independent of the luminous matter in galaxies. Each galaxy whose motion is measured, serves as a test particle of the gravitational field around it. With large numbers of accurately measured objects it is possible reconstruct the mass distribution of material in the Universe. Unfortunately, this has not been easy – since the first results of 15 years ago of the "Great Attractor" (Lynden-Bell et al. 1988), the field has been littered with contradictory results and findings that are still not understood. The heart of the problem has been finding a way to obtain large numbers of accurate distances between $0 < cz < 10{,}000$ km s^{-1}. GSAOI can make significant progress in this field by measuring *H* band surface brightness fluctuation (SBF) distances to hundreds of galaxies in this range. Already SBF has been used at optical wavelengths to probe motions at $cz < 2000$ km s^{-1}, but this work was hampered by the fact that much of the action happens outside of 2000 km s^{-1} (Tonry et al. 2000).

H band surface brightness fluctuations (Jensen et al. 2001) provide distances accurate to ~ 0.12 mag, and are limited, in the case of GSAOI, by contamination from globular clusters at $cz > 8000$ km s^{-1}, not by photometric uncertainty. Using observations of ~ 100 SBF galaxies in the direction of the Great Attractor, the location, mass, and extent of the Great Attractor could finally be ascertained by looking at the motion of galaxies on all sides of this object. An additional survey of ~ 500 galaxies at $cz < 6000$ km s^{-1} across the whole sky would provide a new scale measurement of bulk motions in the current Universe, and provide a measurement of the scales over which dark matter clusters.

2.16.2 Sensitivity Limit

A 0.12 mag *H* band SBF measurement requires reaching $H \sim 23$ mag with a signal to noise ratio of 10. GSAOI can reach this level of sensitivity in ~ 0.4 hr of integration time. This level of integration is appropriate for nearly all the galaxies in the bulk motion sample. In total, we estimate that this program needs ~ 200 hr of integration time to carry out its objectives, although the program could be expanded to any amount of observing time by increasing the sample of galaxies.

2.16.3 Guide Star Availability

There are tens of thousands of acceptable galaxies at $cz < 6000$ km s^{-1}, and therefore it is possible to choose those galaxies that have appropriate guide stars.

2.16.4 Special Requirements

A uniform PSF over the GSAOI field is required to accurately measure the surface brightness fluctuations. The large field of GSOAI also would allow multiple galaxies to be imaged simultaneously in those nearby clusters and groups that have appropriate guide stars.

2.17 The Formation of the Disks of Disk Galaxies

2.17.1 Science Goal

The formation of the disks of disk galaxies remains poorly understood. Cold Dark Matter (CDM) simulations have difficulty in reproducing the observed properties of disks. For example:

- The disks that are formed in the simulations have significantly smaller scale lengths and less angular momentum than real galactic disks.

- Many disk galaxies have only the thin disk component, with no bulge or significant thick disk. This means that they formed in a very quiescent way, with no star formation occurring before the gas disk had settled. Furthermore, since the epoch of disk settling, there cannot have been any significant disturbance by the mergers and interactions that are such a feature of the CDM simulations.

Other important problems include:

- Almost all disk galaxies have an exponential radial surface brightness distribution. The reason for this exponential form is not known; nor is it known when the exponential form is established.

- The exponential disks are typically truncated radially at a radius of about 3 exponential scale lengths. This truncation is an important and probably fundamental indicator of the nature of the galaxy formation process. At this time, the reason for the truncation is not known. Here are some of the many possibilities:
    - The truncation may reflect the maximum angular momentum of baryons in the protogalaxy, or
    - It may be caused by tidal interactions of lumps of dark + baryonic matter early in the hierarchical aggregation process, or
    - It may be the radius where the gas density goes below the critical density for star formation, or
    - It may be associated with the viscous evolution of the star-forming disk (which itself may also lead to the exponential light distribution).

Almost everything that we know about galactic disks comes from disks at low redshift, so little is known about when the fundamental properties of the disks were established. MCAO gives us the opportunity to study the detailed structure of galactic disks at earlier epochs, to a redshift $z = 1$.

The primary goal is to see if the exponential nature of the disks, their characteristic scale lengths and their truncation are already established at $z = 1$. To achieve this goal, we need the high spatial resolution and high near-infrared sensitivity offered by the GSAOI. Observationally, we would aim to study galaxies over a range of redshifts, but at the same rest-frame mean wavelength. We would compare low redshift galaxies observed in the *I* band with galaxies at $z = 0.5$ in the *J* band and at $z = 1$ in the *H* band.

Resolution: For a disk galaxy like the Milky Way, with a scale length of 4 kpc, the expected truncation radius at $z = 1$ in a standard Λ-universe is about 1.8″. Such galaxies are very well suited to surface photometry in *J* and *H* with GSAOI.

Near-infrared imaging: For low redshift spirals, the large scale structure of the disk depends on wavelength. This is partly due to the star formation history and partly to internal absorption. We therefore need to compare low and higher redshift galaxies with observations at the same rest-frame mean wavelength. Although one could cover the redshift range $z = 0$ to 1 using observations in *B* and *I*, this would be far from ideal; dust and star formation affect the surface photometry much more at shorter wavelengths. It is better to make the low redshift observations in the *I* band and the higher redshift observations in the near-infrared.

We would propose to survey disk galaxies in the field and in a sample of clusters, at redshifts around $z = 0.5$ (*J*), $z = 1$ (*H*) and $z = 1.7$ (*Ks*).

2.17.2 Sensitivity Limit

The goal is to do surface photometry of our disk galaxies out to a radius of ~ 3.5 scale lengths. We estimate the required integration times, assuming conservatively that the intrinsic (rest-frame) central surface brightness of our galactic disks is independent of redshift and similar to that most commonly seen among normal low redshift disks ($\mu_I = 19.8$ mag arcsec^{-2} or 1.5×10^{-17} erg cm^{-2} s^{-1} Å^{-1} arcsec^{-2}). We also assume that the typical exponential scale length is 4 kpc. Using ellipse-fitting surface photometry, with 6 radial bins extending out to 3.5 scale lengths, and requiring a signal-to-noise ratio of 3 in the outermost bin, we would need an integration time of ~ 30 min at *J* for the $z = 0.5$ galaxies and 3.5 hr at *H* for the $z = 1$ galaxies.

For disks of normal rest-frame surface brightness, the observed surface brightness at $z = 1.7$ is too faint for us to do this kind of photometry in the *K* band. However, if the rest frame surface brightness is one magnitude brighter than the value adopted above, *K* band surface photometry becomes possible; an integration time of 3.5 hr is needed to achieve a signal-to-noise ratio of 3 at 3.4 scale lengths. We note that (i) many low redshift galaxies do have central surface brightnesses that are brighter than the standard value adopted in the previous paragraph; (ii) the intrinsic surface brightness of disks at $z = 1.7$ may well be higher than at $z = 0$, depending on their star formation history.

2.17.3 Guide Star Availability

This project can be done in any high latitude fields so galaxies will be selected based on proximity to suitable guide stars.

2.17.4 Special Requirements

Uniformity of the PSF over the GSAOI field is very desirable for deriving the surface brightness profiles.

2.18 Exploring Dark Energy Via High Redshift Supernovae

2.18.1 Science Goal

Type Ia supernovae have emerged as one of the sharpest tools in the astrophysicist's shed for measuring extragalactic distances, with a precision of ~ 6%. These exploding stars have shown, through observations made by the High-Z SN Search Team and the Supernova Cosmology Project that the Universe is accelerating in its expansion, a result that indicates the cosmos must be filled with some previously unknown form of dark energy. By studying Type Ia supernovae with GSAOI we can accurately trace the cosmic expansion to $z \sim 2$, learning key physical properties of the dark energy.

Different types of dark energy affect the rate at which the Universe expands depending on their effective equation of state. For example, the cosmological constant has an equation of state, $w \equiv \rho/p = -1$, where as quintessence – a scalar field – has $w > -1$. Each variant of dark energy has it own evolving equation of state that produces a signature in the Hubble diagram of the SNe Ia. With current instrumentation, we can find and follow SNe Ia to $z = 1.1$. To move beyond this redshift, we need an instrument with near-infrared sensitivity such as GSAOI.

Complementary optical spectral observations of the host galaxy are useful to accurately measure the redshift of the SN.

2.18.2 Sensitivity Limit

Table 5 lists the brightness at maximum light of a SN Ia as a function of redshift assuming a Lambda Cosmology ($\Omega_\Lambda = 0.7$, $\Omega_M = 0.3$). The integration time needed to adequately detect it with GSAOI is also tabulated. It is apparent that SNe can be measured in the *H* band to $z > 2$ using GSAOI.

To achieve an accurate (~ 0.2 mag) distance measurement, each SN must be observed in two bands at maximum light with a total signal-to-noise ratio of all observations combined > 20. In addition, they should be followed for > 15 days in the rest frame at approximately five epochs with a signal-to-noise ratio > 5, at which point they will be ~ 0.7 mag fainter than at maximum light. A sample of > 10 objects is required to adequately constrain the SN Ia Hubble diagram at $z > 1.1$. In total, this program will require approximately 40 nights of observing time.

Table 5: Predicted SN Ia Magnitudes

Redshift	SN Ia Brightness				GSAOI Imaging Time (hrs)				Total Integration Time per SN
	Z	***J***	***H***	***K***	***Z***	***J***	***H***	***K***	**(hrs)**
1.2	23.8	23.6	23.6		0.2	1.4	1.4		14.5
1.3	24.2	23.8	23.7		0.3	2.1	1.7		19.5
1.4	24.5	23.9	23.7		0.6	2.5	1.7		22.0
1.5		24.1	23.7	23.8		3.6	1.7	3.6	28.7
1.6		24.3	23.8	23.9		5.2	2.1	4.4	30.0
1.7		24.5	23.9	24.1		7.6	2.5	6.3	40.3
1.8		24.6	23.9	24.2		9.1	2.5	7.6	45.4
1.9		24.8	24.1	24.2		13.2	3.6	7.6	52.1
2.0		24.9	24.2	24.2		15.8	4.4	7.6	56.5

2.18.3 Guide Star Availability

Supernovae can be discovered either using HST+WFPC3/ACS in pre-selected locations that have guide stars. Recent work with HST has demonstrated that two images, separated by 1 month in the rest frame will yield 1 SN Ia per 50 square arcminutes to $z < 2$. A HST program with ACS can survey to $Z = 26$ mag in 3 orbits and therefore uncover 1 SN Ia to $z < 2$ per 15 orbits.

Alternatively, GSAOI could be used to search around pre-selected guide stars for very distant SNe Ia at $z \sim 2$ in the *H* band using its full 85″×85″ field-of-view; a perfect PSF is not necessary for SN discovery. The rate of discovery in this mode will be ~ 1 SN per ~ 40 hr of integration time. This could be achieved through utilizing observations from other programs as appropriate.

2.18.4 Special Requirements

A uniform PSF across the GSAOI field is required to accurately measure the SN photometry as it rises and falls in its brightness. The observations need broad band filters that are matched to their optical rest frame equivalent. For example, for a SN at $z = 1.9$, *H* band matches rest frame *V* band.

2.19 Science Risks

2.19.1 Sensitivity

Many of the GSAOI/MCAO science drivers are extremely demanding on the limiting magnitude that must be achieved. If this faint limiting magnitude is not achieved, some of these programs cannot be addressed at all.

2.19.2 Guide Star Availability

MCAO requires three natural guide stars within its field with $R \leq 19$ mag. For previously identified specific objects, guide star availability imposes an important constraint on object selection. However, many of the science programs can use field centers that are chosen to be near suitable guide stars. These programs will be only minimally affected by guide star availability.

3 Simulations

3.1 Imager Performance Predictions

The performance simulation program developed for NIFS has been adapted to provide performance predictions for GSAOI. This program, *gsaoisim*, has been used to predict the imager performance, to define a suitable pupil-viewer scale, and to identify the optimal image scale for the GSAOI OIWFS. These simulations are described below. They serve to constrain design parameters for the instrument and provide a realistic framework in which to assess the science drivers for the instrument.

3.1.1 Performance Model

The GSAOI performance simulator, *gsaoisim*, is derived from the NIFS performance simulator, *nifssim*. The program simulates a 64×64 pixel image by calculating the expected signal photo-current from a celestial object and adding to this the detected currents from various noise sources. The input parameters used in the performance model are summarized in Table 6.

Table 6: Model Input Parameters

Parameter	Value	Unit	Description
RN	5	e	Detector read noise
D	50000	e	Detector well depth
T_{max}	3600	s	Maximum integration time
T_{cry}	65	K	Cryostat temperature
λ_{max}	2.60	μm	Detector sensitivity cutoff
Q	0.60		Detector quantum efficiency
T_{win}	275	K	Window temperature
ε_{win}	0.01		Window emissivity
T_{aos}	275	K	AOS temperature
ε_{aos}	0.15		AOS emissivity
τ_{aos}	0.85		AOS transmission
T_{tel}	275	K	Telescope temperature
ε_{tel}	0.044		Telescope emissivity
τ_{tel}	0.956		Telescope transmission
T_{sky}	260	K	Sky temperature
W_h	0.4	arcsec	Seeing FWHM
S	0.2,0.4,0.6		Strehl ratio at J, H, K

3.1.1.1 Noise Sources

3.1.1.1.1 Detector Read Noise

The GSAOI imager detector will be a mosaic of Rockwell 2040×2040 HAWAII-2RG devices with 18 μm pixels. The read noise, *RN*, is expected to be ~ 10 e for a single non-destructive read (NDR). However, it should be possible to reduce this to ~ 5 e using ~ 16 NDRs using Fowler sampling. We adopt the lower value. The detector well depth is assumed to be D = 50,000 e. This is a conservative figure: Rockwell specify 100,000 e. The maximum integration time will be set by the background brightness and variability. We adopt t_{max} ~ 3600 s.

3.1.1.1.2 Detector Dark Current

The dark current, I_{dc}, for the HgCdTe/CdZnTe MBE detector is uncertain, but is expected to be lower than for the PACE technology HAWAII-2 and HAWAII-1 devices. In any case, dark current is not a significant noise source for the GSAOI imager. We adopt a value of $I_{dc} = 0.05$ e s^{-1} pix^{-1}.

3.1.1.1.3 Cryostat Thermal Emission

Each pixel views 2π steradians of the cryostat interior that is effectively radiating with unit emissivity as a blackbody at the cryostat temperature, T_{cry}. This emission occurs after the filter so the detector sees broad-band emission extending to the detector cutoff wavelength, $\lambda_{max} = 2.60\ \mu$m for a HAWAII-2RG array. The detector quantum efficiency, Q, is taken to be that of the HAWAII-1 array published on the WWW pages of the Rockwell Science Center and shown in Figure 11. This detector quantum efficiency is ~ 60% over most of the 1-2.5 μm wavelength range. Rockwell CdZnTe/MBE technology devices are expected to have higher quantum efficiency due to the better lattice match of CdZnTe with HgCdTe compared to PACE devices. Quantum efficiencies of > 85% may be achieved over the 1.0-2.5 μm wavelength range with MBE devices. This potential gain has not been included in our simulations.

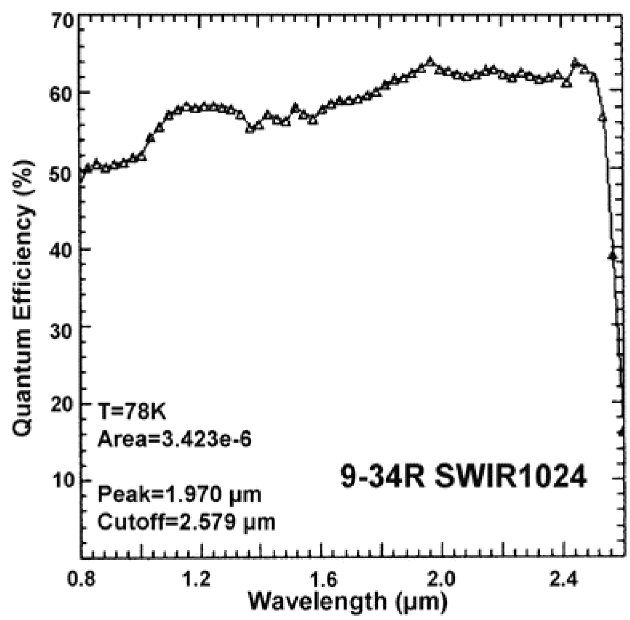

Figure 11: Quantum efficiency for a HAWAII-1 array (Rockwell WWW pages).

Cryostat thermal emission produces a photo-current of

$$I_{cry} = \int_0^{\lambda_{max}} \frac{6.00\times10^{22} A_{pix}\pi}{\lambda^4(\mu\mathrm{m})\left[e^{14388/\lambda(\mu\mathrm{m})/T_{cry}} - 1\right]} d\lambda(\mu\mathrm{m}) Q \ \ \mathrm{e\ s^{-1}\ pix^{-1}}$$

where A_{pix} is the detector pixel size in cm^2. This photo-current for a detector cutoff wavelength of 2.6 μm is shown in Figure 12 as a function of T_{cry}. Ideally, the cryostat thermal emission photo-current should be insignificant compared to the detector dark current, so it must be below ~ 0.05 e s^{-1} pix^{-1}. This requires T_{cry} < 150 K. A duplicate of the NIRI/NIFS cryostat will reach a temperature below 70 K.

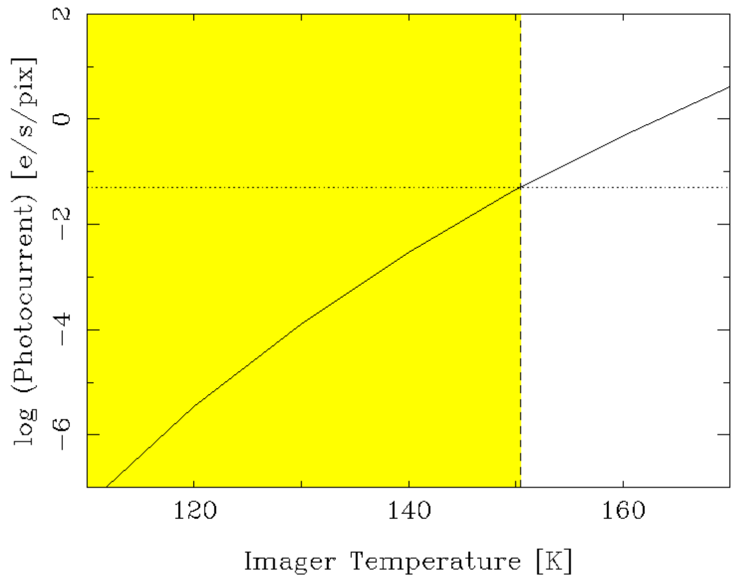

Figure 12: Cryostat thermal photo-current versus cryostat temperature for a 2.6 μm detector cutoff wavelength.

3.1.1.1.4 Window Thermal Emission

Dust on the cryostat window is a source of thermal emission. We assume that the window has an emissivity of ε_{win} = 0.01 and a temperature of T_{win} = 275 K. Thermal emission from the cryostat window generates a photo-current of

$$I_{win} = \varepsilon_{win} \frac{6.00\times10^{22} A_{tel}\Omega_{pix}\Delta\lambda(\mu\text{m})}{\lambda^4(\mu\text{m})\left[e^{14388/\lambda(\mu\text{m})/T_{win}}-1\right]}\tau_{ima}Q \ \text{ e s}^{-1}\text{ pix}^{-1}$$

where A_{tel} is the telescope collecting area in cm^2, Ω_{pix} is the solid angle on the sky subtended by one pixel, $\Delta\lambda$ is the spectral bandpass, and τ_{ima} is the transmission of the GSAOI imager. GSAOI has 0.02″ pixels. We adopt standard *ZJHK* broad-band filters. The GSAOI imager transmission as a function of wavelength is shown in Figure 13.

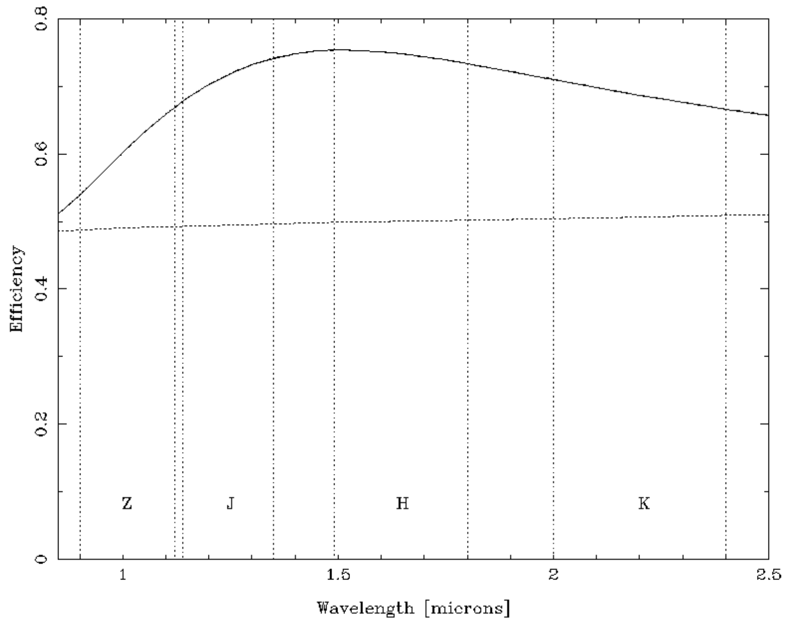

Figure 13: GSAOI imager transmission excluding telescope, AO system, filter, and detector with (*solid line*) and without (*dotted line*) anti-reflection coatings. The wavelength ranges of the broad-band filters are indicated.

3.1.1.1.5 MCAO Thermal Emission

The MCAO science path emissivities with and without an atmospheric dispersion corrector (ADC) have been estimated in Table 6 of the MCAO PDR documentation and are repeated in Table 7. We adopt a "typical" emissivity of $\varepsilon_{aos} = 0.15$, a transmission of $\tau_{aos} = 0.85$, and an operating temperature of $T_{aos} = 275$ K. Thermal emission from the MCAO science path generates a photo-current of

$$I_{aos} = \varepsilon_{aos} \frac{6.00 \times 10^{22} A_{tel} \Omega_{pix} \Delta\lambda(\mu\text{m})}{\lambda^4(\mu\text{m})\left[e^{14388/\lambda(\mu\text{m})/T_{aos}} - 1\right]} \tau_{ima} Q \ \text{e s}^{-1} \text{ pix}^{-1}.$$

Table 7: MCAO Throughput and Emissivity

	Throughput			Emissivity
Wavelength (μm)	1.00	1.65	2.20	2.20
Overall without ADC	0.768	0.845	0.858	0.139
Overall with ADC	0.742	0.802	0.821	0.183

3.1.1.1.6 Telescope Thermal Emission

The telescope M1, M2, and M3 mirrors are assumed to use protected silver coatings with a single surface reflectivity of 98.5%. This gives a combined emissivity of $\varepsilon_{tel} = 0.044$, a combined transmission of $\tau_{tel} = 0.956$, and we adopt a typical night-time operating temperature of $T_{tel} = 275$ K. Thermal emission from the M1, M2, and M3 telescope mirrors generates a photo-current of

$$I_{tel} = \varepsilon_{tel} \frac{6.00 \times 10^{22} A_{tel} \Omega_{pix} \Delta\lambda(\mu\text{m})}{\lambda^4(\mu\text{m})\left[e^{14388/\lambda(\mu\text{m})/T_{tel}} - 1\right]} \tau_{aos} \tau_{ima} Q \ \text{e s}^{-1} \text{ pix}^{-1}.$$

3.1.1.1.7 Airglow Line Emission

Sky emission is significant at near-infrared wavelengths. Airglow emission, mainly due to OH molecules, is dominant shortward of ~ 2.27 μm and thermal emission from the sky contributes at longer wavelengths. Airglow line-emission data are based on a tabulation of typical line strengths provided by François Piche which is based on the data of Maihara et al. (1993) and Oliva & Origlia (1992). These data have been checked for order of magnitude consistency with the atmospheric emission spectrum provided on the Gemini WWW pages, and have been extended into the *K* band with additional line strength and wavelength data chosen to mimic this Mauna Kea emission spectrum.

3.1.1.1.8 Airglow Continuum Emission

A knowledge of the atmospheric continuum emission between strong airglow emission lines is needed for predicting performance in the *J* and *H* bands. This is poorly known and difficult to distinguish empirically from instrumental scattered light. Sobolev (1978) reported an airglow continuum emission of 300-600 photon s^{-1} m^{-2} arcsec^{-2} μm^{-1} in the *J* band. McCaughrean (1988) estimated the airglow continuum to be 280 photon s^{-1} m^{-2} arcsec^{-2} μm^{-1} in the *H* band. Maihara et al. (1993) measure a continuum of 580 photon/s/m^2/arcsec^2/μm at 1.665 μm but found higher values on moon-lit nights. We adopt the latter value at all wavelengths and note that the precise value is not important since other continuum sources dominate.

3.1.1.1.9 Sky Thermal Emission

Thermal emission from the sky will also produce continuum emission with increasing importance towards longer wavelengths. We assume a typical sky temperature of T_{sky} = 260 K and base the adopted sky emissivity, ε_{sky}, on Mauna Kea atmospheric transmission data, τ_{sky}, available from the Gemini WWW pages. Thermal emission from the sky generates a photo-current of

$$I_{sky} = \varepsilon_{sky} \frac{6.00\times10^{22} A_{tel}\Omega_{pix}\Delta\lambda(\mu\mathrm{m})}{\lambda^4(\mu\mathrm{m})\left[e^{14388/\lambda(\mu\mathrm{m})/T_{sky}} - 1\right]} \tau_{tel}\tau_{aos}\tau_{ima}Q \text{ e s}^{-1}\text{ pix}^{-1}.$$

3.1.1.2 Signal Currents

3.1.1.2.1 Point Spread Function

The signal-to-noise ratio achieved by GSAOI on point sources depends on the PSF, $P(\theta)$; poorer images spread light over more detector pixels. MCAO will deliver a complex image to GSAOI. We approximate $P(\theta)$ by a diffraction-limited core, $P_c(\theta)$, and a seeing-limited halo, $P_h(\theta)$. The diffraction-limited core is modeled with an Airy function modified to allow for the telescope central obstruction (Schroeder 1987):

$$P_c(\theta) = \frac{1}{(1-\varepsilon^2)^2}\left[\frac{2J_1(\upsilon)}{\upsilon} - \varepsilon^2\frac{2J_1(\varepsilon\upsilon)}{\varepsilon\upsilon}\right]^2$$

where J_1 is the Bessel function of order one, ε is the ratio of the central obstruction radius to the primary mirror radius, and

$$\upsilon = \frac{2\pi R_P\theta}{\lambda}$$

where R_P is the primary mirror radius, θ is the angle on the sky, and λ is the wavelength. The seeing halo is modeled by a Moffat function with index of 11/6 as suggested by Racine et al. (1999) based on results from the AO Bonnette on CFHT:

$$P_h(\theta) = \left[1 + \frac{11}{6}\left(\frac{\theta}{W_h}\right)^2\right]^{-11/6}$$

where W_h is the seeing FWHM. The contribution of each profile is set by the Strehl ratio, *S*, such that

$$\alpha = \frac{\sum_c - S\sum_h}{S\left(\sum_c - \sum_h\right)}$$

and

$$P(\theta) = \frac{\alpha P_c(\theta) + (1-\alpha)P_h(\theta)}{\alpha\sum_c + (1-\alpha)\sum_h}$$

where Σ_c and Σ_h are the total counts in the core and halo templates, respectively. We define baseline observing conditions to correspond to Strehl ratios of 0.2, 0.4, and 0.6 in the *J*, *H*, and *K* bands, respectively, and a seeing FWHM of 0.4″.

The quoted Strehl ratios are those derived from the Gemini top-down image quality error budget in median seeing conditions (Oschmann 1997, Gemini System Error Budget Plan, SPE-S-G0041) and are similar to those derived in the MCAO image quality error budget (MCAO PDR Documentation, Table 2). The Strehl ratio degradation is due to a combination of uncorrected seeing and optical aberrations in the telescope, MCAO, and the science instrument. This analytical PSF is similar to the predicted MCAO PSFs, but has the advantage that the effects of different diffraction core widths and Strehl ratios can be modeled easily.

3.1.1.2.2 Point Sources

The source signal current, $I_{sig}(\theta)$, is derived from the source brightness specified in magnitudes, m, and converted to flux density using the absolute flux calibration of Bersanelli et al. (1991) which is based on a Vega effective temperature of 11200 K:

$$F_{\lambda,0} = \frac{1.653\times10^{-12}}{\lambda^5(\mu m)\left[e^{1.2848/\lambda(\mu m)} - 1\right]} \text{ W cm}^{-2}\ \mu\text{m}^{-1},$$

$$I_{sig}(\theta) = P(\theta)\frac{\lambda}{hc}F_{\lambda,0}10^{-0.4m}A_{tel}\Delta\lambda\tau_{sky}\tau_{tel}\tau_{aos}\tau_{ima}Q \text{ e s}^{-1}\text{ pix}^{-1}.$$

3.1.1.3 Simulated Images

The total detected signal, S_{tot}, is given by

$$S_{tot} = \left(I_{sig} + I_{sky} + I_{OHL} + I_{OHC} + I_{OHS} + I_{tel} + I_{aos} + I_{win} + I_{cry} + I_{dc}\right)T \quad \text{e pix}^{-1}$$

where T is the integration time. To this is added statistical noise which is derived from random Gaussian deviates with standard deviation, N, given by

$$N = \left(RN^2 + S_{tot}\right)^{1/2}$$

for each pixel in a 64×64 pixel simulated image.

3.1.2 Imager Pixel Scale

The optimal spatial pixel scale for the GSAOI imager is a compromise between adequately sampling the diffraction-limited image core and providing sufficient field-of-view to satisfy the science requirements. The FWHM of the diffraction-limited image core will be ~ 0.06″ in the *K* band and less at shorter wavelengths. Nyquist sampling this image requires a pixel size of ~ 0.03″. Nyquist sampling *J* band images requires a pixel size of ~ 0.015″, which leads to a field size of only ~ 60″×60″. This field-of-view is smaller than the AO-corrected MCAO field. We adopt a compromise pixel size of 0.02″ that adequately samples diffraction-limited images at long wavelengths where MCAO performs best and provides a field-of-view that is well-matched to the MCAO corrected field.

3.1.3 Imager Performance Estimates

3.1.3.1 Limiting Magnitudes

Limiting magnitudes for a total on-source integration time of 1 hr in 0.4″ seeing through a 0.08″×0.08″ square aperture are listed for each filter in Table 8 along with the Strehl ratio that was assumed for that filter and the sky brightness that resulted.

Saturation magnitudes for each filter are also listed in Table 8. These are calculated for an assumed minimum integration time of 5 s and a detector full-well depth of 50,000 e. The same 0.4″ seeing and Strehl ratios listed in Table 8 apply. The faint broad-band saturation magnitudes present a calibration problem: faint near-infrared photometric standards typically have $K \sim$ 10-12 mag (e.g., Persson et al. 1998). It will be necessary to read out only a sub-region of the imager detector so as not to saturate these standard stars. The brightest Persson et al. (1998) standards can be recorded in a 512×512 sub-region (10.2″×10.2″) that is read out 16 times faster than the full array using an integration time of 0.3 s.

Table 8: Imager Sensitivities (10:1 in 1 hr)

Filter	Limiting Magnitude (mag)	Saturation Magnitude (mag)	Assumed Strehl Ratio	Sky Brightness (mag/arcsec^2)
Z	24.9	13.2	0.2	17.2
J	23.5	12.6	0.2	14.9
H	23.5	12.9	0.4	13.9
Ks	23.2	12.3	0.6	13.4
K	23.2	12.2	0.6	13.3
J continuum	22.4	10.2	0.2	15.0
H continuum	22.4	10.4	0.4	14.1
CH_4 (short)	23.0	11.9	0.4	13.9
CH_4 (long)	22.9	11.7	0.4	13.8
Ks continuum	22.2	9.9	0.6	13.8
Kl continuum	21.9	9.6	0.6	13.5
He I 1.0830 μm	22.9	10.3	0.2	16.0
H I Pγ	22.9	10.3	0.2	16.1
H I Pβ	21.8	10.1	0.2	13.9
[Fe II] 1.644 μm	22.1	10.3	0.6	13.7
H_2O	22.8	10.4	0.6	14.4
H_2 1-0 S(1)	22.0	9.9	0.6	13.4
H I Brγ	22.1	9.6	0.6	13.7
H_2 2-1 S(1)	22.0	9.7	0.6	13.5
CO 2-0 (bh)	21.8	9.6	0.6	13.3
CO 3-1 (bh)	21.6	9.5	0.6	13.0

3.1.3.2 Dominant Noise Sources

Modeled background signals for each filter with an integration time of 600 s are listed in Table 9. The dark current is assumed to contribute 30 e/pix in this integration time. It is clear from Table 9 that airglow line emission dominates for all broad-band filters and most narrow-band filters. Thermal emission from the MCAO system makes a significant contribution in the two broad *K* bands and is dominant in the longer wavelength narrow-band filters. These background signals ensure that GSAOI will be background limited in all broad-band filters in integration times > 30 s and in all narrow-band filters in integration times > 150 s with a read noise of 10 e; many filters will be strongly background limited in these times.

Table 9: Imager Background Contributions (600 s)

Filter	Airglow (e/pix)	Sky Thermal (e/pix)	Telescope Thermal (e/pix)	MCAO Thermal (e/pix)	Window Thermal (e/pix)	Total (e/pix)
Z	2152	0	0	0	0	2182
J	11182	0	0	0	0	11212
H	25130	1	4	13	1	25180
Ks	12822	236	1394	4289	276	19049
K	11007	554	2421	7448	483	21945
J continuum	1132	0	0	0	0	1162
H continuum	1873	0	0	0	0	1903
CH_4 (short)	8942	0	0	1	0	8973
CH_4 (long)	9465	0	2	5	0	9501
Ks continuum	1248	8	63	193	12	1554
Kl continuum	212	64	342	1053	68	1770
He I 1.0830 μm	423	0	0	0	0	453
H I Pγ	381	0	0	0	0	411
H I Pβ	2867	0	0	0	0	2897
[Fe II] 1.644 μm	2621	0	0	0	0	2652
H_2O	1032	40	39	121	8	1269
H_2 1-0 S(1)	1875	4	88	271	17	2285
H I Brγ	796	8	115	353	23	1325
H_2 2-1 S(1)	491	37	284	874	57	1774
CO 2-0 (bh)	65	90	414	1273	83	1954
CO 3-1 (bh)	66	139	531	1634	107	2507

3.1.3.3 Imager On-Detector Guide Window Performance

The imager ODGW performance has been estimated using the imager performance model to generate star frames that have then been centroided and the RMS centroiding accuracy determined from 200 simulated guide star frames. Limiting magnitudes that achieve a centroiding accuracy of ~ 2 mas (i.e., 0.1 pix) in integration times of 0.01 s and 30 s are listed for each broad-band filter in Table 10.

Table 10: Imager ODGW Sensitivities (2 mas RMS)

Filter	Limiting Magnitude 10 ms integration (mag)	Limiting Magnitude 30 s integration (mag)
Z	13.9	22.0
J	13.1	21.2
H	12.7	20.5
Ks	12.0	19.8
K	11.9	19.7

3.2 Imager Pupil-Viewer Scale

GSAOI will use a pupil viewer to image the internal cold stop on the imager detector. The pupil viewer will be used both to align the instrument with the MCAO system and to identify and then eliminate sources of extraneous background emission. Consequently, the cold stop image should have a scale that is fine enough to accurately align the cold stop with the MCAO system, but also coarse enough to detect sources of background emission.

3.2.1 Optimal Scale

Predicted background contributions in each filter were tabulated in Table 9. This table shows that background signals of ~ 20000 e/pix are expected at *H*, *Ks*, and *K* in a 600 s integration. Background signals of ~ 2000 e/pix will be recorded in an integration time of 1 min, which is more appropriate for alignment/test integrations. This background emission is detected by all ~ 4500×4500 equivalent pixels passed by a 90″×90″ field mask, so the total background signal passing through the cold stop is ~ 4×10^{10} e.

If the pupil image is centered in the detector, the gaps between the four detectors block some of the pupil image. The ISS can be rotated to record views of the telescope at other orientations, but the central ~ 2.5 mm (~ 140 pixels) of the pupil image will never be recorded. Maximizing the diameter of the pupil image minimizes the impact of this vignetting. Such images are expected to be signal shot noise limited so there will be no penalty incurred in rebinning finely sampled pixels in software.

We therefore adopt a pupil image diameter of ~ 3800 pixels. One pixel then corresponds to ~ 0.3 mm at the secondary mirror and ~ 2.1 mm at the primary mirror, (although the resolution of the pupil-viewer optics will not be this good). The 2.5 mm gap between the detectors blocks the equivalent of ~ 140 pixels, or strips 292 mm wide at the primary mirror and 37 mm wide at the secondary mirror. This is ~ 1/3 of the diameter of the secondary mirror obstruction. For comparison, NIRI uses a pupil viewer with an image diameter of ~ 940 pixels.

The expected background signals and signal-to-noise ratios obtained with this pupil image size through each of the broad-band filters are listed in Table 11. These signals are appropriate for a well depth of ~ 50,000 e and the background signal is consequently detected with good signal-to-noise ratio.

Table 11: Pupil Viewer Performance (1 min integration, 3800 pixel diameter)

Filter	Background Signal (e/pix)	SNR (/pix)
Z	390	18
J	2000	44
H	4500	66
Ks	3400	57
K	3920	62

3.2.2 Instrument Alignment

The internal cold stop is required to be aligned with the MCAO exit pupil to better than 1% of the pupil diameter. A cold stop image with a diameter of ~ 200 pixels would be sufficient to meet this requirement. However, finer sampling is desirable. The proposed diameter of 3800 pixels is excellent for this purpose.

3.2.3 Star Light

The high background signal in the pupil image will make it difficult to detect a single star (although it is not obvious why anyone would want to do this). A star that produces a signal in the pupil image equal to the total background signal over the full field would produce a total signal of ~ $3{,}500\times\pi/4\times(3800)^2 = 4\times10^{10}$ e. With a system efficiency of ~ 30%, this corresponds to *K* ~ 4.0 mag.

3.3 Imager Non-Common-Path Phase Errors

Imaging performance is improved if the MCAO deformable mirror that is conjugated to ground level (DM0) can be configured to correct non-common-path wave-front phase errors introduced by the GSAOI imager optics. Normally, the MCAO Diagnostic Wave-Front Sensor is used to flatten the wave front exiting the MCAO system. It is preferable to ensure that the wave front reaching the imager detector is flat. This will be achieved by recording images on either side of focus and analyzing them in the manner described by Roddier & Roddier (1993). This is similar to the procedure used in the wave-front curvature sensor of Hokupa'a. The light source for these images will be the MCAO NGS source simulator. This is a 5×5 grid of fiber-fed sources that will produce separate images at the GSAOI imager detector. These images will be defocused using the convex and concave defocus lenses in the imager utility wheel. The images will be analyzed using the Roddier program, and actuator offsets calculated from fitted low-order Zernike polynomials characterizing the wave-front error will be input to the MCAO system.

3.3.1 Methodology

The methodology has been described by Roddier et al. (1990). The illumination I_1(r) is measured in a plane P_1 at distance l in front of focus and the illumination I_2(r) is measured in plane P_2 at distance l behind focus (Figure 14). Local errors in the wave-front curvature cause rays to converge closer to one plane than the other, and so enhance the illumination in one plane and degrade the corresponding illumination in the other plane. In this way, the differences in illumination between the two out-of-focus images measure the local wave-front curvature. If f is the focal length of the telescope and $l \ll f$, then from geometrical optics

$$\frac{\Delta I}{I}(\rho) = 2\frac{\lambda f^2}{lR^2}\nabla^2 Z(\rho)$$

where $I = (I_1+I_2)/2$ is the average illumination, ρ is a position vector in the telescope pupil expressed in units of the pupil radius, R is the pupil radius, and Z is the wave-front surface in units of the wavelength, λ. Radial wave-front tilts at the pupil edge produce local shifts at the edge of the beam cross sections. These shifts produce a narrow edge signal in the difference image proportional to the radial wave-front tilts. The general wave-front reconstruction method consists of computing the wave-front shape from the curvatures by solving a Poisson equation with the radial edge tilts as boundary conditions.

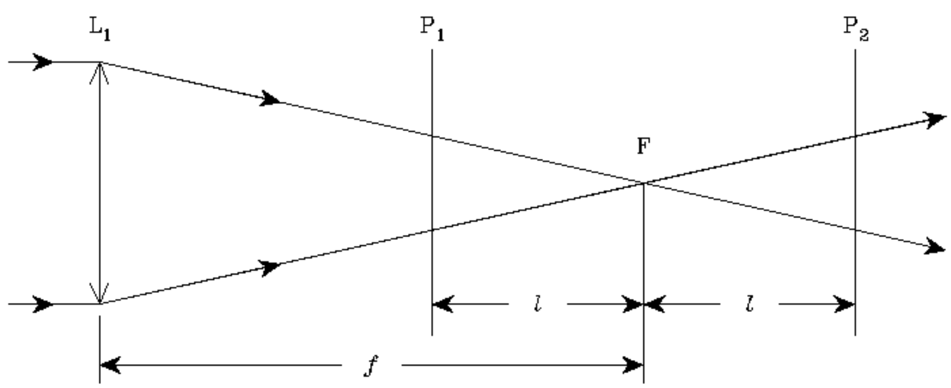

Figure 14: Parameters used in the non-common-path phase error analysis. The primary mirror is at L_1, the focal plane is at *F*, and defocused images are recorded at planes P_1 and P_2 distance *l* in front of and behind focus.

3.3.2 Optimal Defocus

The illumination in plane P_1 can be considered as a pupil image that is blurred by the imager PSF. If α is the FWHM of the MCAO image core, then the blur size is $\alpha(f\text{-}l) \approx \alpha f$. This blur should be small compared to the scale a of the wave-front structures that are to be measured. Since in the image at P_1 this structure is scaled down by a factor of l/f relative to the primary mirror, we require that

$$\alpha f << \frac{al}{f}$$

or that the amount of defocus

$$l >> \frac{\alpha f^2}{a}.$$

For the MCAO f/34 focus, $\alpha = 0.06''$ in the K band and $f = 272$ m. The MCAO inter-actuator spacing maps to 500 mm at the telescope primary mirror. The MCAO deformable mirror DM0, which is conjugated to the telescope primary mirror, cannot correct wave-front structure on smaller scales than this so $a = 500$ mm. Then $l >> 43.0$ mm. If we aim for a wave-front resolution of ~ 200 mm at the 8 m primary mirror, then we require that $l \sim 108$ mm.

This is an optimal value. Increasing l further increases the wave-front resolution, but reduces the intensity contrast of the illumination variations, as can be seen from the equation for $\Delta I/I$.

3.3.3 Illumination Source

It is proposed to use the MCAO NGS source simulator as the illumination source for measuring non-common-path phase errors. The 5×5 array of 4 μm diameter fiber-optic sources has a separation of ~ 16.5″ referred to the sky.

Images defocused by 108 mm from the f/34 focal plane have a diameter of ~ 3.18 mm (176 pixels), which corresponds to 2.4″ on the sky. Consequently, it will be possible to record separate defocused images from each of the 5×5 array of NGS simulators, and so derive wave-front phase errors from a variety of field positions.

The brightness of the NGS source simulators is a concern. If they saturated an in-focus image (50,000 e in 4 pixels) in 10 s, say, the defocused image would record only 8 e/pix. Increasing the integration time to 600 s gives a signal of ~ 480 e/pix for a SNR per pixel of ~ 22. Failing this, defocused images of stars will have to be used.

3.4 OIWFS Pixel Scale

3.4.1 Centroiding Error Simulations

GSAOI will use an OIWFS in one of two monitoring modes. In one, the OIWFS will monitor slow tip-tilt and focus variations. Slow tip-tilt variations are primarily due to instrumental flexure. Slow focus variations are primarily due to changes in the height of the atmospheric sodium layer in which the MCAO laser guide stars are formed. In the other mode, the OIWFS will monitor fast tip-tilt and focus variations. In this mode, the OIWFS acts as a natural guide star WFS for the MCAO system. The OIWFS uses a four-facetted Shack-Hartmann prism. This produces four images of the guide star at the OIWFS detector. The mean displacement of the four images senses tip-tilt variations. The separations of the four images sense focus changes in two directions.

GSAOI is an adaptive-optics instrument so it must perform at the diffraction limit in order to realize the full potential of the MCAO system. The GSAOI FPRD effectively requires that the GSAOI OIWFS maintains the centroid of a star image to < 0.1 pixels (2 mas) over a period of 1 hr. Furthermore, the image Strehl ratio due to GSAOI should be > 0.94. This demands that focus variations are monitored and corrected at the 0.1 pixel level as well.

To a large extent, the scientific scope of MCAO and GSAOI will be defined by guide star availability. Consequently, it is imperative that the OIWFS be optimized to use the faintest possible guide stars while achieving this demanding performance.

3.4.1.1 Approach

The GSAOI OIWFS centroiding performance has been modeled using a modified version of *gsaoisim*. The centroid of each simulated image is determined using an implementation of the centroiding algorithm used by the Gemini A&G IOC software to centroid OIWFS data. A 12×12 pixel centroiding window is used. This is consistent with the number of pixels that can be read out at 200 Hz for each of the four images formed by the real OIWFS. Typically 200 images have been synthesized and centroided for each parameter set, and the RMS centroiding accuracy has been determined directly from the centroiding results. The true centroid of the simulated star image is dithered randomly by ±0.5 pixels to avoid imposing a particular pixel geometry on the result. (The different centroiding accuracies obtained for odd versus even numbers of pixels, i.e., centroiding to a pixel center or boundary, has been noted previously by Jenkins 1996). We note that it will not be possible to arrange all four real OIWFS images to land at inter-pixel boundaries and hence to operate as quadrant detectors.

3.4.1.2 Guide Star Image

The OIWFS image shape is not set solely by the MCAO system, but rather includes the effect of diffraction at the OIWFS Shack-Hartmann prism, which divides the pupil into four quadrants. We follow the lead of Jenkins (1996) and approximate the diffraction-limited part of the profile by an Airy function appropriate to a 4 m diameter circular pupil. We further assume that the 2× broader profile width results in a 4× reduction in profile height (i.e., effective Strehl ratio) in order to maintain total flux. The seeing-limited halo is assumed to be unaffected by prism diffraction. The intensity of the whole profile is reduced by a further factor of four to account for the smaller effective pupil size per image. We caution that the long-term average AO-corrected PSF is not necessarily appropriate for fast tip-tilt/focus simulations. These images may consist of multiple speckles.

A more accurate estimate of the diffraction-limited OIWFS PSF has been obtained by Fourier transforming the telescope pupil to form its image, inverse Fourier transforming this to simulate the pupil formed at the four-facetted Shack-Hartmann prism, masking all but one quadrant of this pupil, and Fourier transforming again to form its image. These images are shown in Figure 15 where it can be seen that the OIWFS PSF (*lower-right* panel) is actually elongated due to the asymmetric pupil. It is, nevertheless, approximately twice the width and 1/16-th of the height of the diffraction-limited image formed by the telescope.

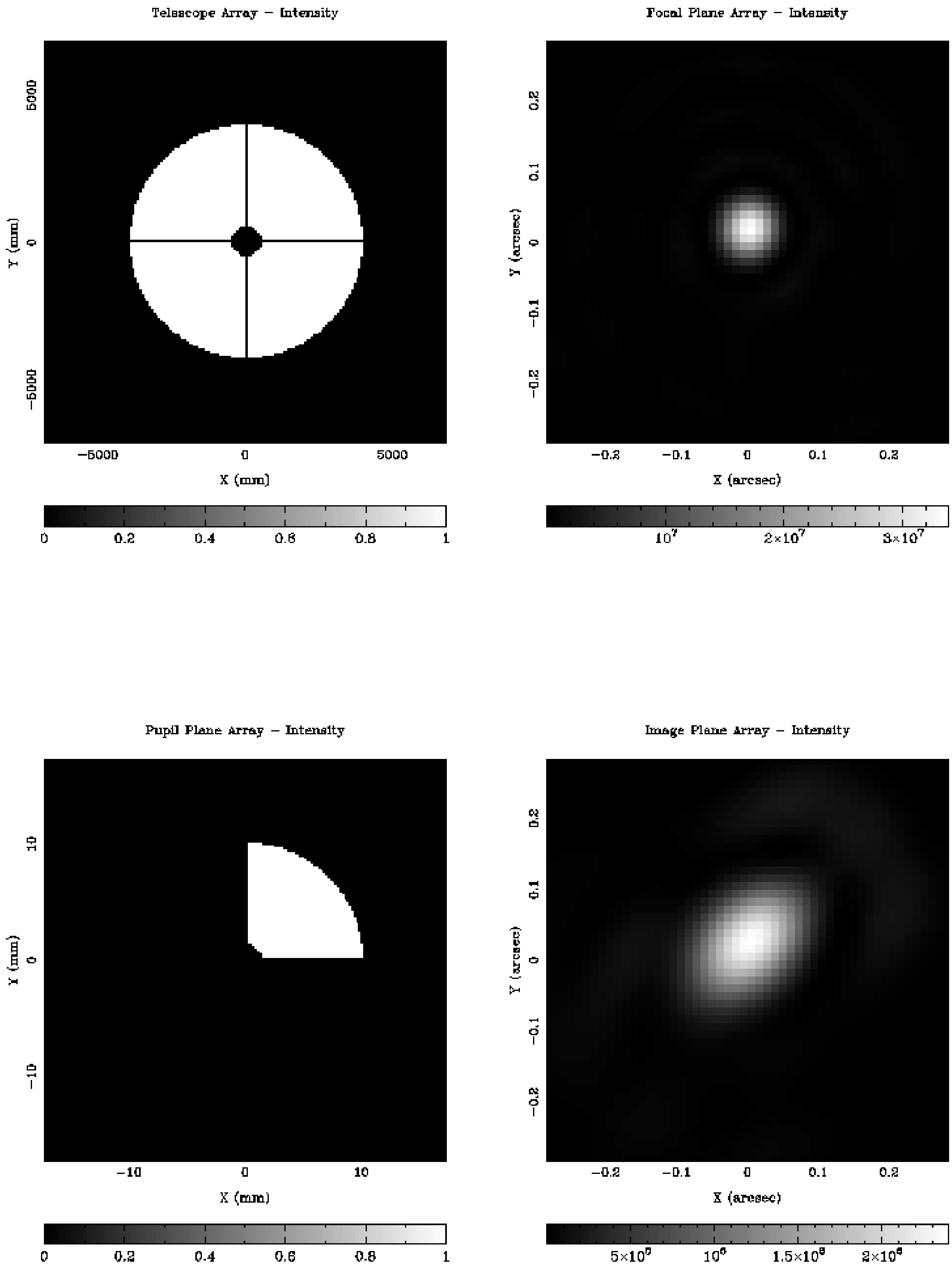

Figure 15: Diffraction-limited *K* band profile of an OIWFS guide star. The telescope pupil is shown at *top-left*. Its image is shown at *top-right*. The pupil passed by the four-facet Shack-Hartmann prism is shown at *bottom-left* and its diffraction-limited image is shown at *bottom-right*.

3.4.1.3 Read Noise

The OIWFS detector read noise is assumed to be 15 e. This is higher than for the imager detector because only single reads are possible at the fast frame rates typical of the OIWFS.

3.4.1.4 Centroiding Algorithm

The centroiding algorithm used is an implementation of the actual algorithm used in the A&G IOC software (Boyer 2001, priv. comm.). The algorithm calculates the intensity-weighted mean pixel number in X and Y for all pixels in a sub-aperture above a threshold value:

$$S_{X,l} = \frac{\sum_{i=1}^{n}\sum_{j=1}^{n}\left(p_{i,j} - T\right)\times i}{\sum_{i=1}^{n}\sum_{j=1}^{n}\left(p_{i,j} - T\right)} - R_{X,l}\,,\ S_{Y,l} = \frac{\sum_{i=1}^{n}\sum_{j=1}^{n}\left(p_{i,j} - T\right)\times j}{\sum_{i=1}^{n}\sum_{j=1}^{n}\left(p_{i,j} - T\right)} - R_{Y,l}$$

where $R_{X,l}$ and $R_{Y,l}$ are the reference coordinates for the l-th sub-aperture, T is the threshold, $p_{i,j}$ is the signal in the pixel at coordinate (i,j) in the l-th sub-aperture, and $(p_{i,j}-T) = 0$ if $p_{i,j} \leq T$.

The threshold level for the NIRI OIWFS is set in the A&G IOC code by sorting the pixel values in the sub-aperture into ascending order and computing

$$T = \left[p_{sorted,h},\ldots,p_{sorted,i}\right] + m \times RMS$$

where h is the first pixel in ascending order to be considered after skipping the lowest valued h-1 pixels, $i = pixelNb*(1.0-R)$, $pixelNb$ is the number of pixels in the sub-aperture, R is a measure of the relative frequency of occurrence of "bright" pixels (which defaults to 0.15), m is a factor (which defaults to 5), and RMS is the root mean squared value of the i-h+1 pixels used in calculating the threshold. In essence, the threshold is ~ 5σ above the mean value of the "sky" pixels in the sub-aperture, after dead pixels have been ignored.

This threshold definition proved to be difficult to implement in our simulation where the pixel size was varied over a large range. In fact, the results are very dependent on the values of R and m that are chosen, and the centroiding algorithm failed under extreme conditions if these parameters were simply fixed.

Consequently, we have adopted different threshold calculations. Initially, we simply adopted the known analytical background and noise levels in the simulation and set the threshold to 5σ above the background. These results are shown in §3.4.3. This simple threshold calculation permits the uncorrected seeing halo to contribute significant weight to the centroid sums when low Strehl ratio PSFs are used. This degrades centroiding performance. Some simulations were repeated later with the centroid sum taken only over the diffraction-limited core out to the first dark ring to overcome this problem.

3.4.2 Centroiding Error Comparisons

3.4.2.1 2.3 m Tip-Tilt Secondary Mirror

Peter Wood (RSAA) performed independent centroiding simulations during the design of the ANU 2.3 m telescope tip-tilt secondary mirror system. He assumed a Gaussian non-AO PSF. The simulations presented here produce a centroiding error that is smaller by ~ 30% than his value for typical input parameters when the AO-corrected PSF used above is replaced by a Gaussian PSF. Our simulations give a centroiding error that is a factor of ~ 2 smaller than Wood's value if we use our AO-corrected PSF. This is to be expected since an Airy function is more peaked than a Gaussian.

3.4.2.2 Close & McCarthy (1994)

Close & McCarthy (1994) describe the FASTTRAC tip-tilt system on the Steward Observatory 2.3 m telescope. They can use guide stars to $K \sim 8$ mag at 100 Hz with a detector read noise of 500 e and 0.5″ or 0.065″ pixels. A precise comparison with this empirical result is difficult. However, our simulation does predict that a star of this magnitude should produce an RMS centroiding error of ~ 0.12″ at 100 Hz with 0.5″ pixels, in reasonable agreement with their assertion.

3.4.2.3 Jenkins (1996)

Charles Jenkins wrote a Gemini memorandum in 1996 that discussed "Optimal pixel sizes in the OIWFS". He presented centroiding accuracy predictions that should be directly comparable to ours. Specifically, he assumed 50% system throughput, a guide star with H = 16.7 mag, a sky background of H = 14.5 mag arcsec^{-2}, a read noise of 10 e, and a frame rate of 50 Hz. Our simulation fails to find a centroid under these conditions (i.e., there is no signal above the adopted threshold). This is reasonable. The total detected signal from a star of this magnitude is ~ 68.2 e and the sky signal in a 0.1″ pixel is 5.2 e, so under these conditions the star is detected with a signal-to-noise ratio per pixel of ~ 2.1 if it is spread over 3×3 pixels and ~ 3.1 if it is spread over only 2×2 pixels. Neither of these is sufficient for a centroid determination (only pixels 5σ above sky are considered).

The origin of our discrepancy with Charles Jenkin's work remains unidentified.

3.4.3 Centroiding Accuracy vs Pixel Scale

RMS centroiding accuracies have been determined for each OIWFS filter for a range of OIWFS pixel scales, guide star brightnesses, and integration times typical of those that will be used by GSAOI in practice.

Figure 16 shows the RMS centroiding accuracy as a function of OIWFS pixel scale for the K filter for integration times of 100 s, 10 s, 1 s, 0.1 s, and 0.01 s. The centroiding accuracy is largely independent of the OIWFS pixel scale over a range of pixel scales. This range is set at the high end by the diffraction-limited core approximately matching the pixel size and at the low end by the diffraction-limited core becoming larger than the 12×12 pixel centroiding window. Large pixels are also more prone to saturating on the background+star signal (open symbols in Figure 16). The general shapes of these curves are in qualitative agreement with those predicted by Charles Jenkins.

The required 2 mas centroiding accuracy is achieved for integration times of 100 s, 10 s, 1 s, 0.1 s, and 0.01 s at $K \sim$ 18.1, 16.9, 15.0, 12.5, and 10.0 mag, respectively, for a pixel size of ~ 60 mas. Note that the limiting magnitude varies in proportion to the integration time for bright guide stars where the signal-to-noise ratio is set by source photon shot noise, and more like the square root of the integration time for faint guide stars where the background is more significant.

Figure 17 shows the RMS centroiding accuracy as a function of OIWFS pixel scale for the H filter for integration times of 100 s, 10 s, 1 s, 0.1 s, and 0.01 s. The required 2 mas centroiding accuracy is achieved at $H \sim$ 18.8, 17.5, 15.5, 13.0, and 10.5 mag in these integration times for a pixel scale of 60 mas. Qualitatively similar features are seen in Figure 16 and Figure 17. The centroiding accuracy degrades sooner at large pixel sizes at the shorter wavelength because the diffraction-limited PSF is smaller at H than K. The degradation at small pixel sizes is also less pronounced because the diffraction-limited PSF is accommodated better within the centroiding window.

Figure 18 shows the RMS centroiding accuracy as a function of OIWFS pixel scale for the J filter for integration times of 100 s, 10 s, 1 s, 0.1 s, and 0.01 s. The required 2 mas centroiding accuracy is achieved at $J \sim$ 18, 16, 14, 13, and 9 mag in these integration times for a pixel scale of 60 mas. However, here we see the centroiding accuracy for bright guide stars, but not faint guide stars, degrading as the pixel size is decreased. This appears to be due to the contribution of the uncorrected seeing halo to the centroiding sum for low Strehl ratio PSFs (0.2 at *J*). This results from fixing the centroiding threshold at 5σ above the analytical sky value.

Figure 19 shows the RMS centroiding accuracy as a function of OIWFS pixel scale for the *Z* filter and integration times of 100 s, 10 s, 1 s, 0.1 s, and 0.01 s. The required 2 mas centroiding accuracy is achieved at *Z* ~ 19.7, 16.5, 14.5, 11.5, and 10.0 mag in these integration times for a pixel scale of 60 mas. Again, the centroiding accuracies obtained appear to be degraded by seeing-halo contamination.

The *J* and *Z* simulations have been repeated using a modified centroiding algorithm in which the centroid sum is taken only over the diffraction-limited core out to the first dark ring. The results for these simulations are shown in Figure 20 and Figure 21. These simulations show qualitatively the same behavior as seen before at *H* and *K*; the centroiding error is fairly insensitive to pixel size until the pixel size exceeds the diffraction core size. The centroiding accuracy degrades more quickly at large pixel sizes using this centroiding algorithm because data beyond the first dark ring are not used. This indicates that the centroiding accuracy achieved at the telescope will be very dependent on the observing conditions and the sophistication of the centroiding algorithm used.

Using the modified centroiding algorithm, the required 2 mas centroiding accuracy is achieved at *J* ~ 19.4, 17.5, 15.5, 13.0, and 10.5 mag in integration times of 100 s, 10 s, 1 s, 0.1 s, and 0.01 s, respectively, for a pixel scale of 60 mas. At *Z*, this accuracy is achieved at *Z* ~ 20, 18, 16, 13, and 11 mag, respectively.

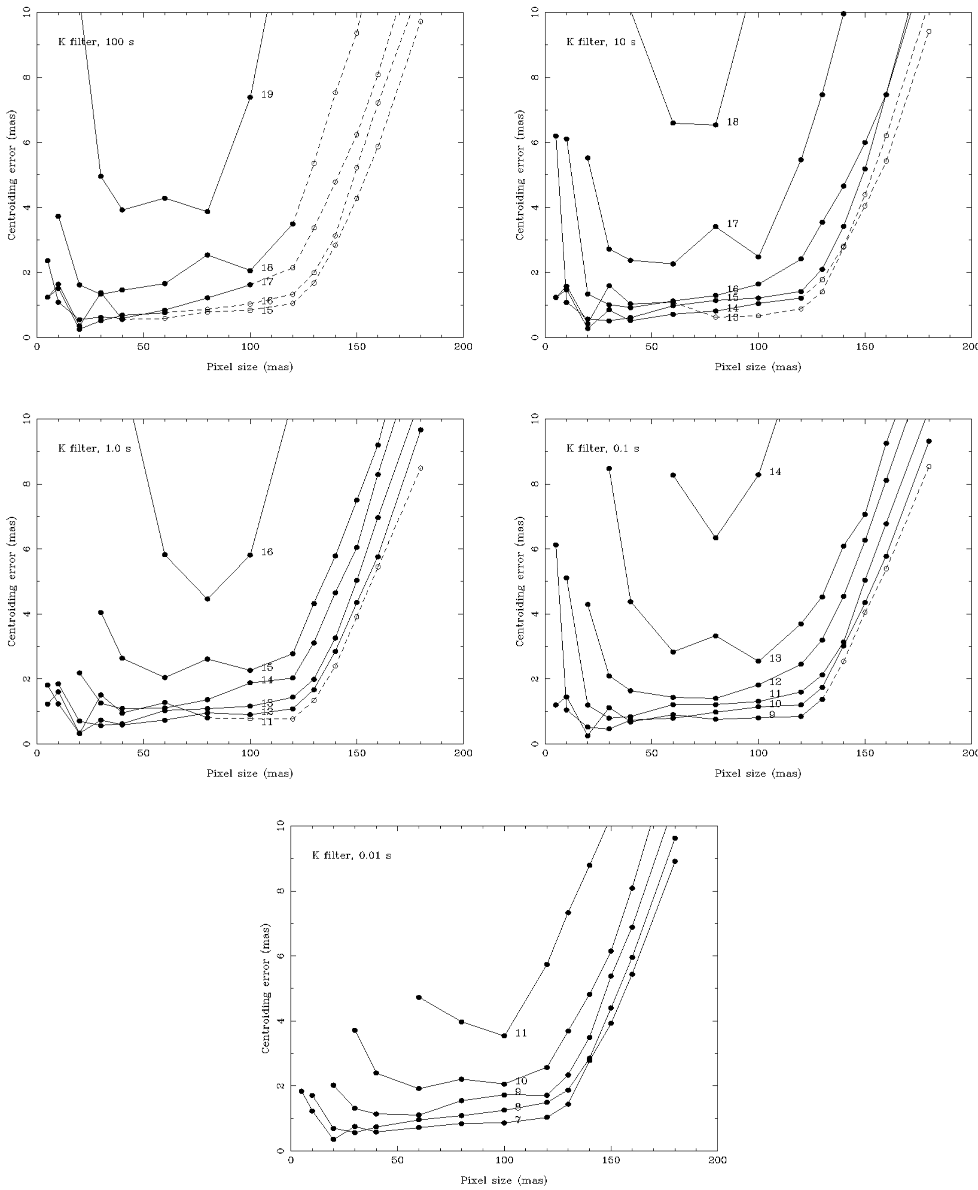

Figure 16: *K* band centroiding error versus OIWFS pixel scale. Results of simulations are shown for OIWFS guide stars with the *K* magnitudes listed at the right of each curve. Results are shown for integration times of 100 s (*top-left*), 10 s (*top-right*), 1 s (*middle-left*), 0.1 s (*middle-right*) and 0.01 s (*bottom-center*). Open symbols indicate exposures that saturate in the specified integration time.

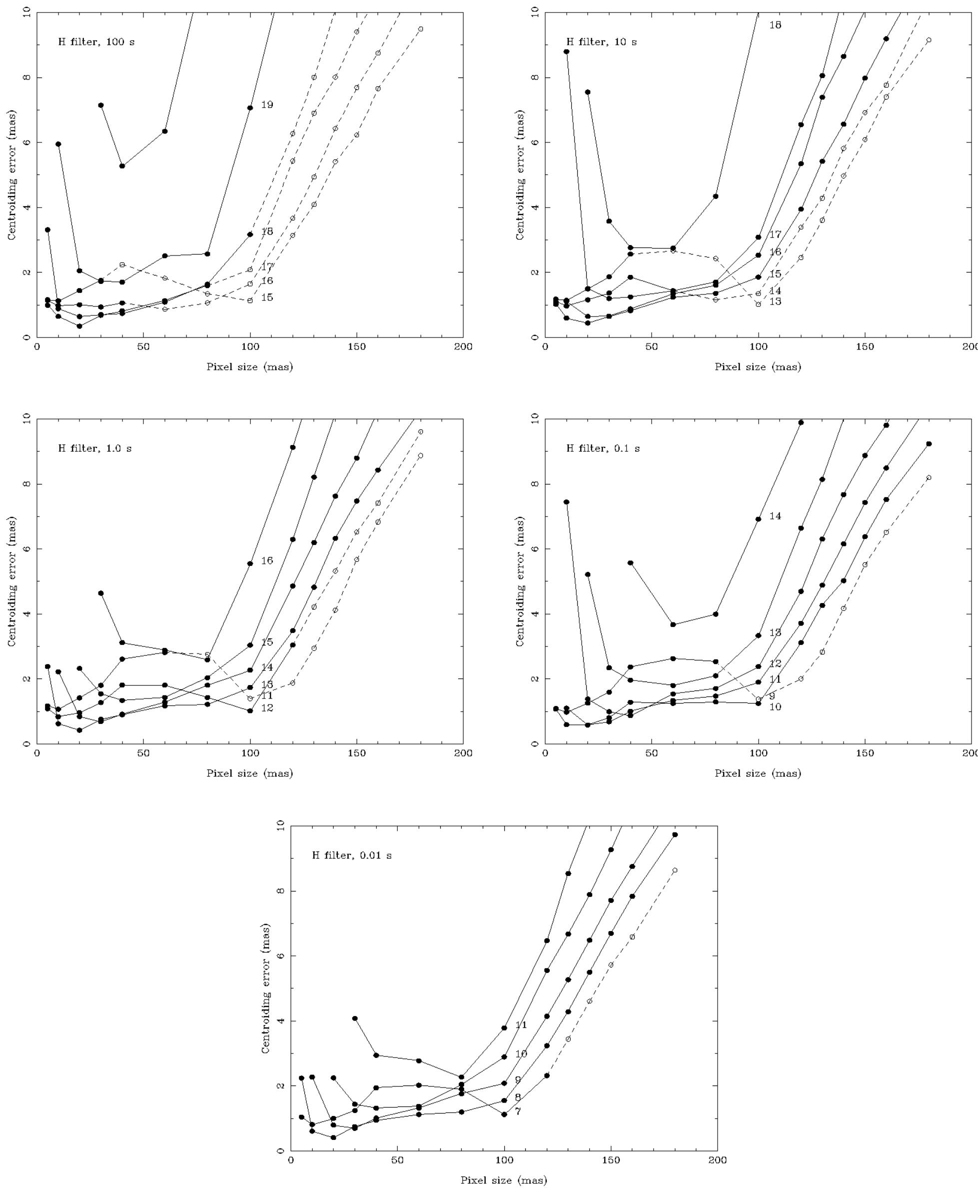

Figure 17: *H* band centroiding error versus OIWFS pixel scale. Results of simulations are shown for OIWFS guide stars with the *H* magnitudes listed at the right of each curve. Results are shown for integration times of 100 s (*top-left*), 10 s (*top-right*), 1 s (*middle-left*), 0.1 s (*middle-right*) and 0.01 s (*bottom-center*). Open symbols indicate exposures that saturate in the specified integration time.

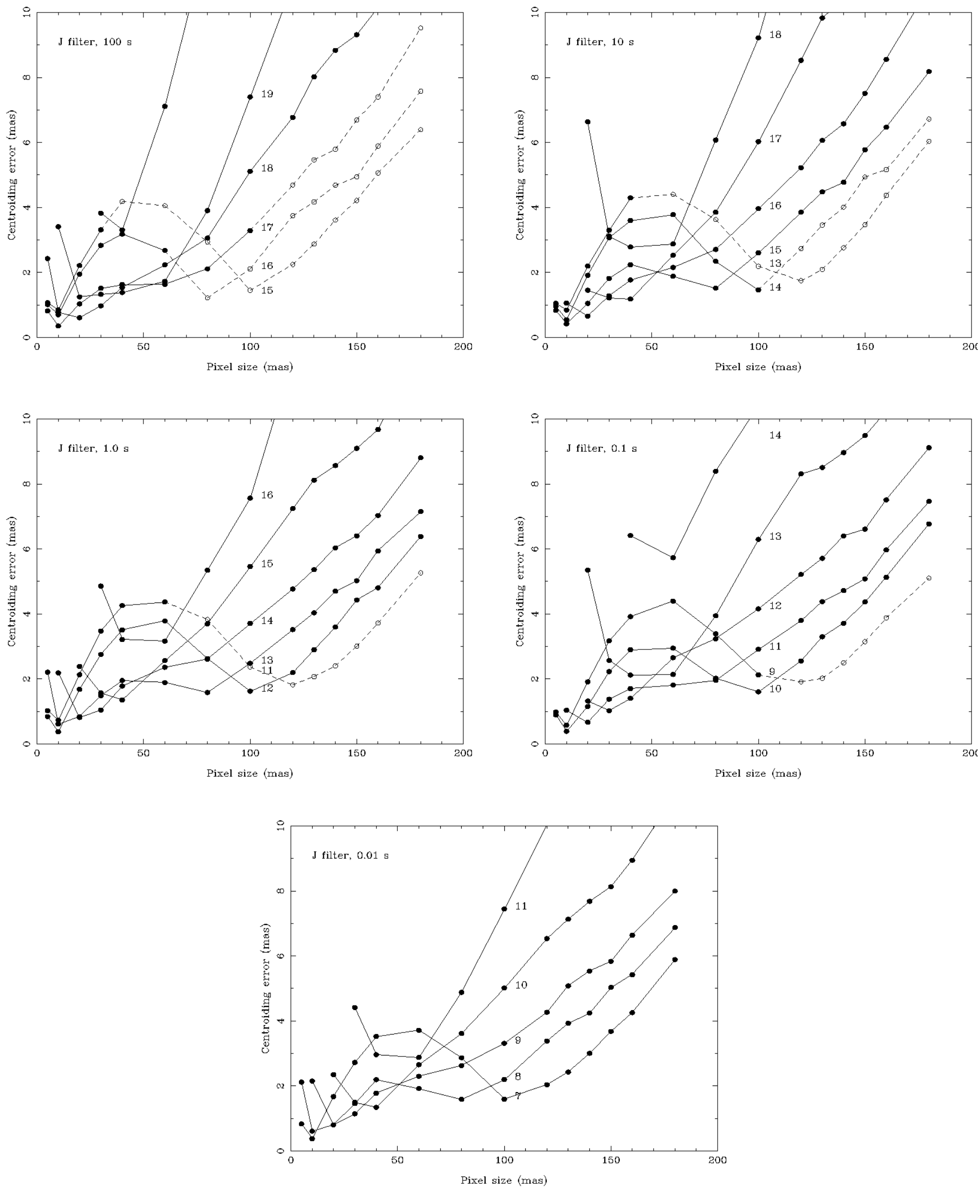

Figure 18: *J* band centroiding error versus OIWFS pixel scale. Results of simulations are shown for OIWFS guide stars with the *J* magnitudes listed at the right of each curve. Results are shown for integration times of 100 s (*top-left*), 10 s (*top-right*), 1 s (*middle-left*), 0.1 s (*middle-right*) and 0.01 s (*bottom-center*). Open symbols indicate exposures that saturate in the specified integration time.

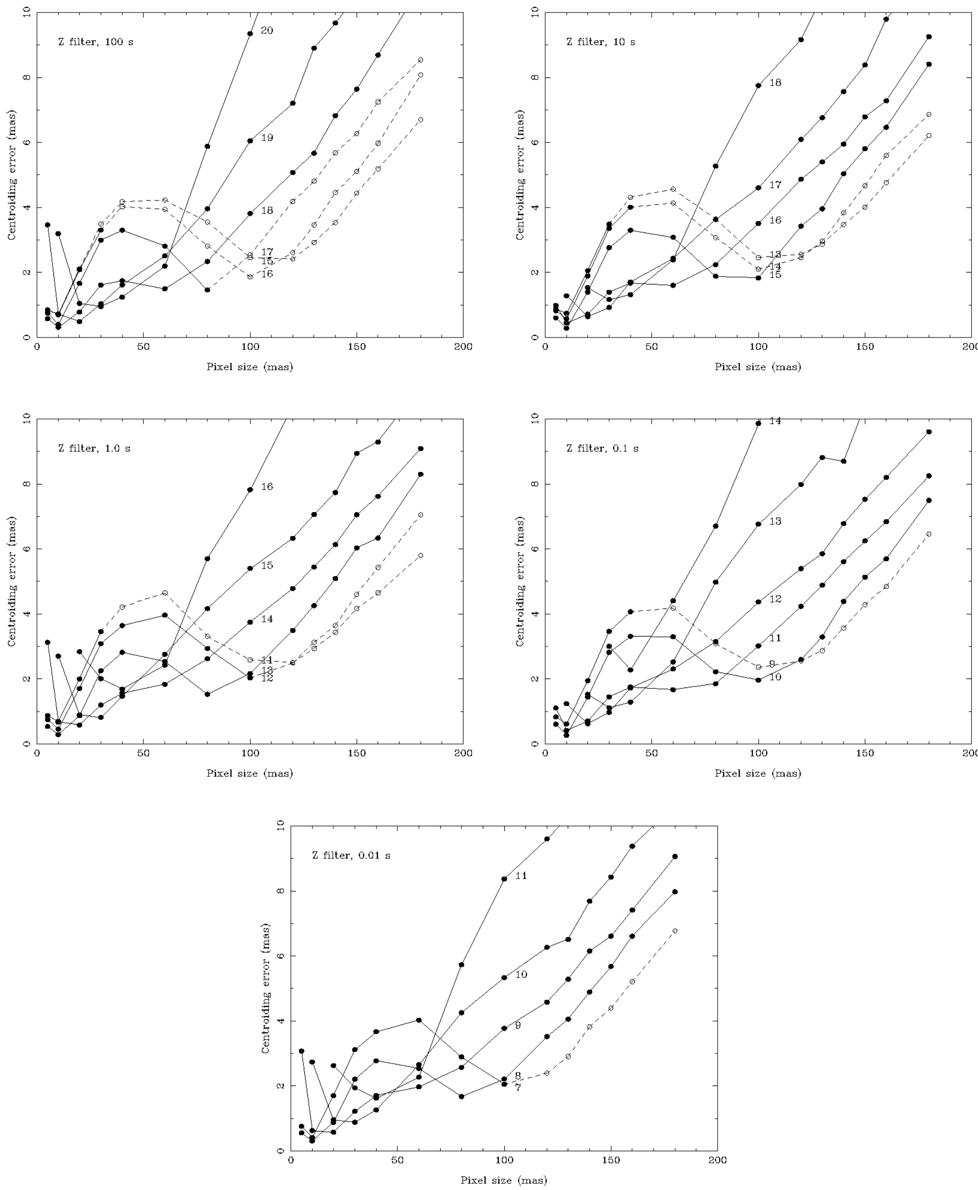

Figure 19: *Z* band centroiding error versus OIWFS pixel scale. Results of simulations are shown for OIWFS guide stars with the *Z* magnitudes listed at the right of each curve. Results are shown for integration times of 100 s (*top-left*), 10 s (*top-right*), 1 s (*middle-left*), 0.1 s (*middle-right*) and 0.01 s (*bottom-center*). Open symbols indicate exposures that saturate in the specified integration time.

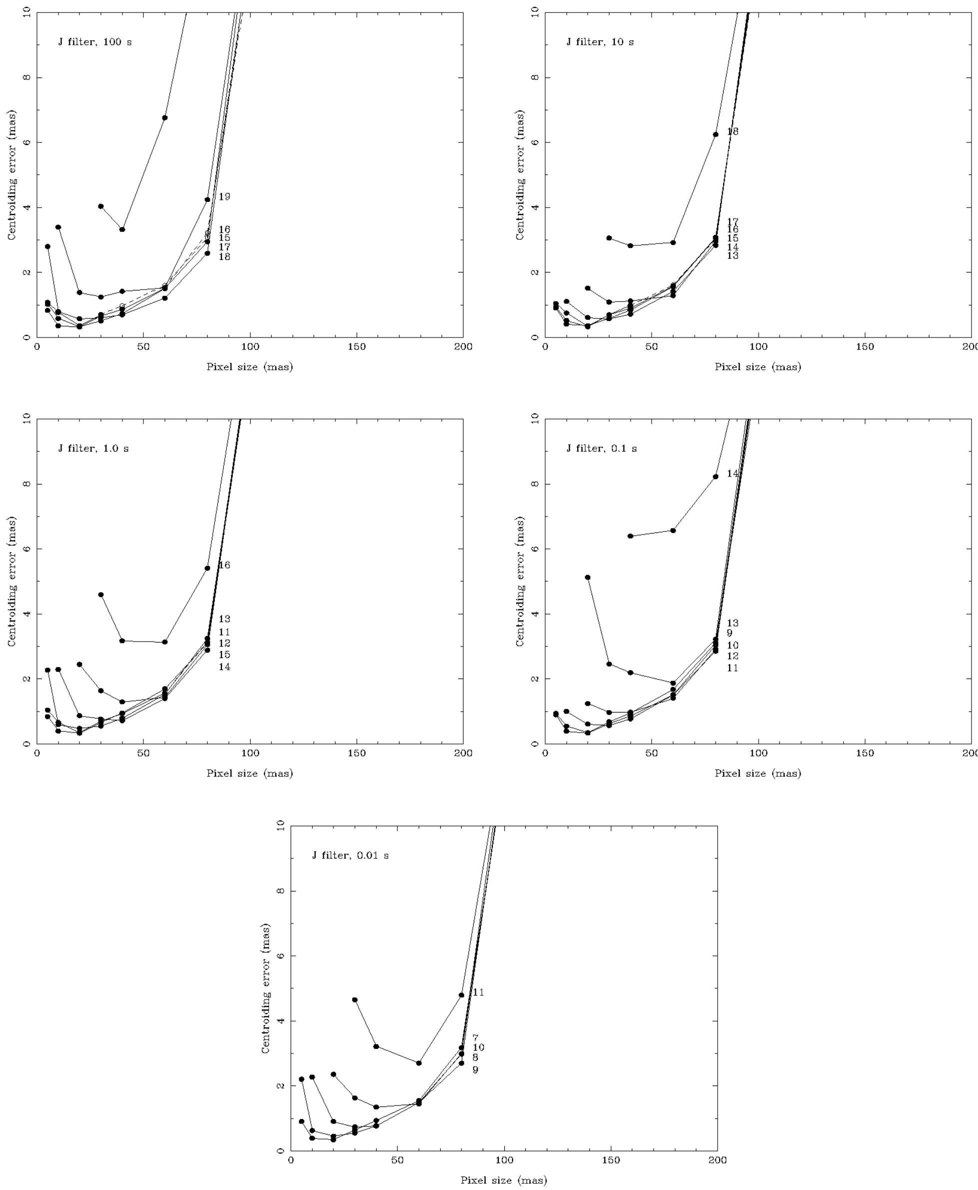

Figure 20: *J* band centroiding error versus OIWFS pixel scale when the centroiding sum is taken only over the diffraction-limited core. Results of simulations are shown for OIWFS guide stars with the *J* magnitudes listed at the right of each curve. Results are shown for integration times of 100 s (*top-left*), 10 s (*top-right*), 1 s (*middle-left*), 0.1 s (*middle-right*) and 0.01 s (*bottom-center*). Open symbols indicate exposures that saturate in the specified integration time.

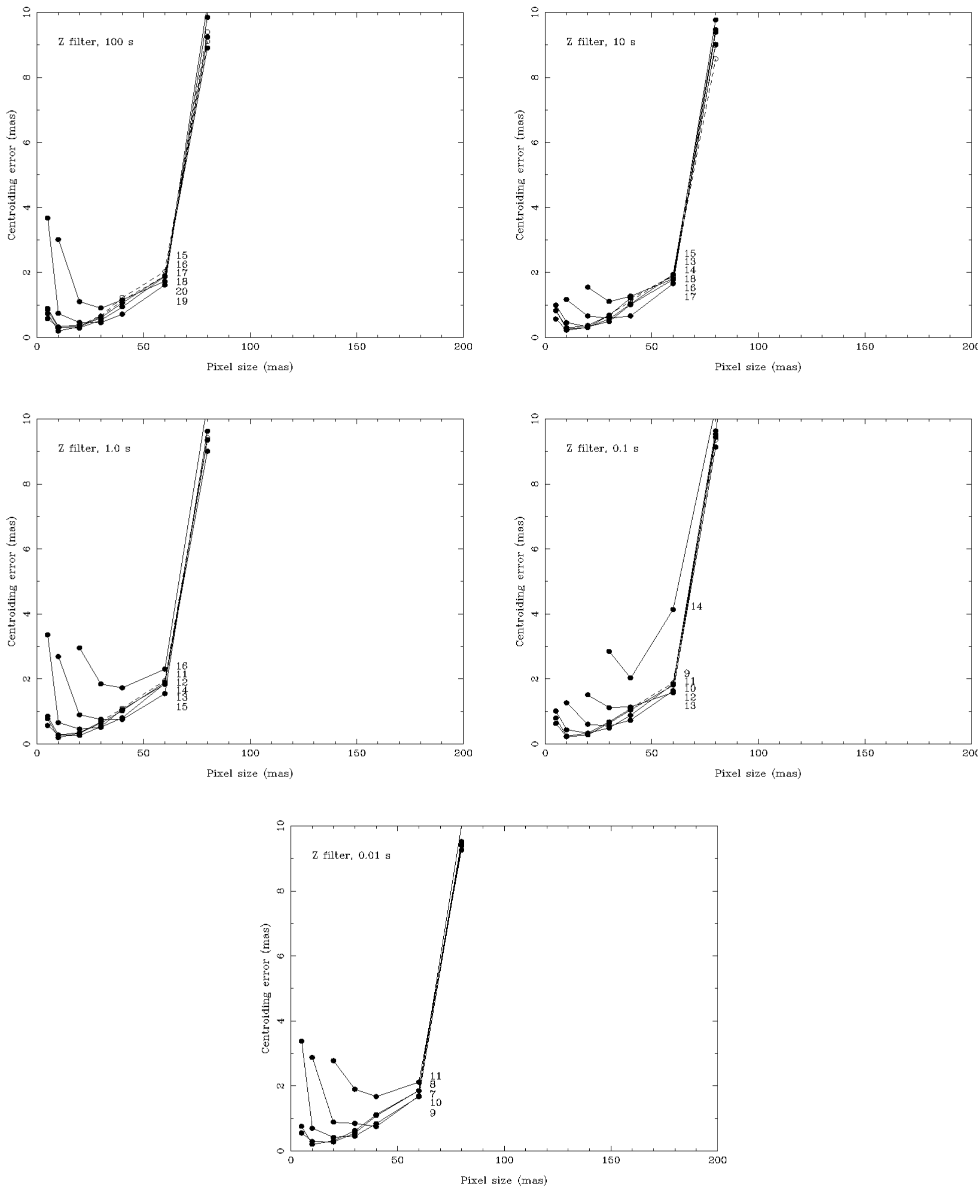

Figure 21: *Z* band centroiding error versus OIWFS pixel scale when the centroiding sum is taken only over the diffraction-limited core. Results of simulations are shown for OIWFS guide stars with the *Z* magnitudes listed at the right of each curve. Results are shown for integration times of 100 s (*top-left*), 10 s (*top-right*), 1 s (*middle-left*), 0.1 s (*middle-right*) and 0.01 s (*bottom-center*). Open symbols indicate exposures that saturate in the specified integration time.

The *K* simulations used a Strehl ratio of 0.6, which is appropriate in good observing conditions. The OIWFS should also perform well in less than ideal conditions. We test this by presenting the results of *K* band simulations with a Strehl ratio of 0.3 in Figure 22. The centering accuracy is more dependent on guide star brightness, but the optimal pixel scale is largely unchanged by the degraded image quality.

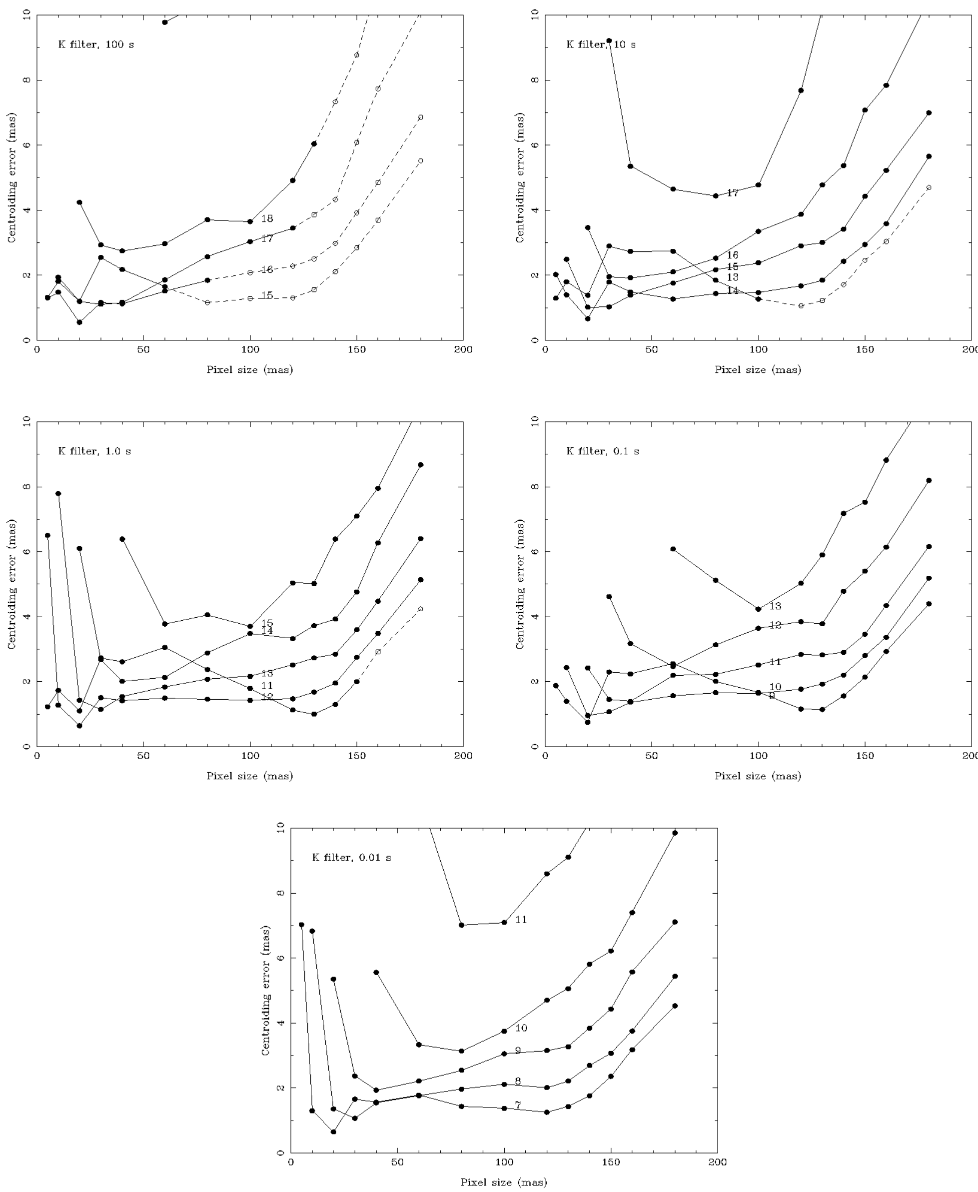

Figure 22: *K* band centroiding error versus OIWFS pixel scale for a Strehl ratio of 0.3. Results of simulations are shown for OIWFS guide stars with the *K* magnitudes listed at the right of each curve. Results are shown for integration times of 100 s (*top-left*), 10 s (*top-right*), 1 s (*middle-left*), 0.1 s (*middle-right*) and 0.01 s (*bottom-center*). Open symbols indicate exposures that saturate in the specified integration time.

These simulations are repeated in Figure 23 using a centroiding algorithm restricted to within the first dark ring of the diffraction-limited core. The behavior is as expected.

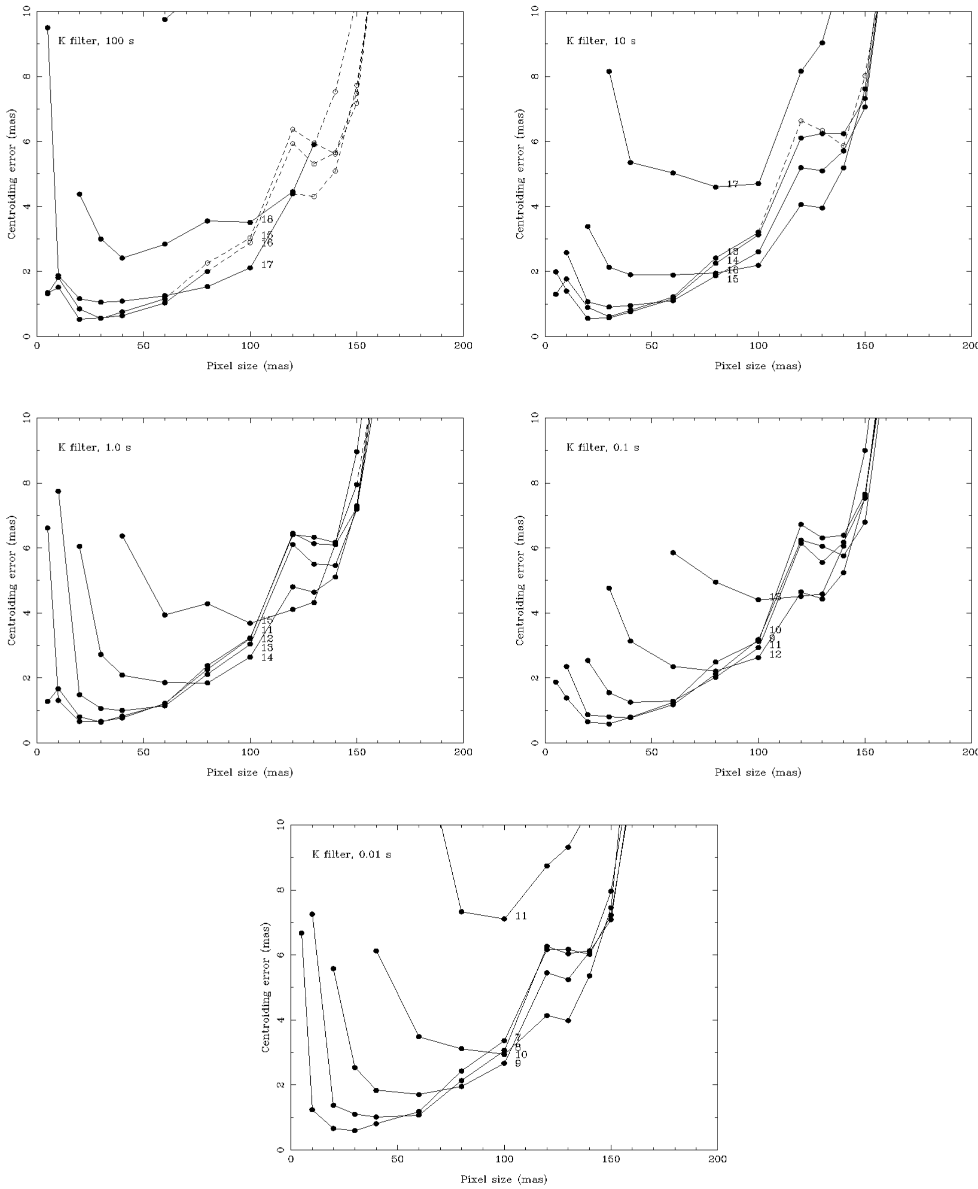

Figure 23: *K* band centroiding error versus OIWFS pixel scale for a Strehl ratio of 0.3 when the centroiding sum is taken only over the diffraction-limited core. Results of simulations are shown for OIWFS guide stars with the *K* magnitudes listed at the right of each curve. Results are shown for integration times of 100 s (*top-left*), 10 s (*top-right*), 1 s (*middle-left*), 0.1 s (*middle-right*) and 0.01 s (*bottom-center*). Open symbols indicate exposures that saturate in the specified integration time.

3.4.4 Optimal Pixel Scale

The results presented in Figure 16 to Figure 21 show that the centroiding accuracy depends on the diffraction core size, and hence on the observation wavelength. The optimal pixel size is a compromise, which we weight towards longer wavelengths where MCAO will perform better. This leads to an optimal OIWFS pixel scale of ~ 65 mas.

3.5 OIWFS Performance Predictions

3.5.1 Limiting Magnitudes

The imager sensitivity model can be used to predict OIWFS sensitivities under the assumptions that both channels have similar throughputs and that the detector read noise is 10 e for single readouts (i.e., no multiple sampling). Allowance is also made for the fact that the OIWFS forms four separate images of each guide star. We further assume that each image must be centroided to an accuracy of 0.002″ (0.1 pix), which is ~ 1/20 of the image FWHM at *H*. We therefore require a signal-to-noise ratio of at least 20 per image per integration. Table 4 lists OIWFS sensitivities for each filter and for integration times of 5 ms (corresponding to fast tip/focus monitoring) and 30 s (corresponding to slow flexure/focus monitoring). It is apparent that full tip-tilt/focus monitoring is possible for only very bright guide stars. Flexure/focus monitoring should be possible on objects approaching the limit of the MCAO NGS sensors. It may be possible to go ~ 1 mag fainter with the OIWFS by using *ZJ* and *HK* filters that combine two standard broad bands.

Table 12: OIWFS Sensitivities (20:1 per image)

Filter	Limiting Magnitude 5 ms integration (mag)	Limiting Magnitude 30 s integration (mag)
Z	10.4	19.6
J	9.9	18.4
H	10.4	18.5
Ks	9.9	18.2
K	9.9	18.1
ZJ	11.0	19.4
HK	11.1	18.9

3.5.2 Guide Star Availability

The availability of faint guide stars at near-infrared wavelengths has been investigated by Spagna[1] for NGST. He tabulates cumulative star counts from which probabilities can be calculated that the 2′ diameter MCAO field for any science object will contain at least one guide star brighter than a particular limit. These probabilities are plotted in Figure 24 where it can be seen that the probability of finding at least one $K \leq 10$ mag guide star in an MCAO field is essentially zero (0.09%) while the probability of finding at least one $K \leq 18$ mag guide star somewhere in the MCAO field is high (99.9% at b = 30º, 88.9% at b = 60º, and 80.3% at b = 90º).

The GSAOI OIWFS field is actually more restricted than the full MCAO field. This may mean that actual guide star availability is less than quoted above. Whether or not this is true depends on whether the science field center can be offset to accommodate the OIWFS guide star, which in turn depends on the science goal.

[1] http://www.ngst.nasa.gov/public/unconfigured/doc_0422/rev_03/NGST_GS_report5.pdf

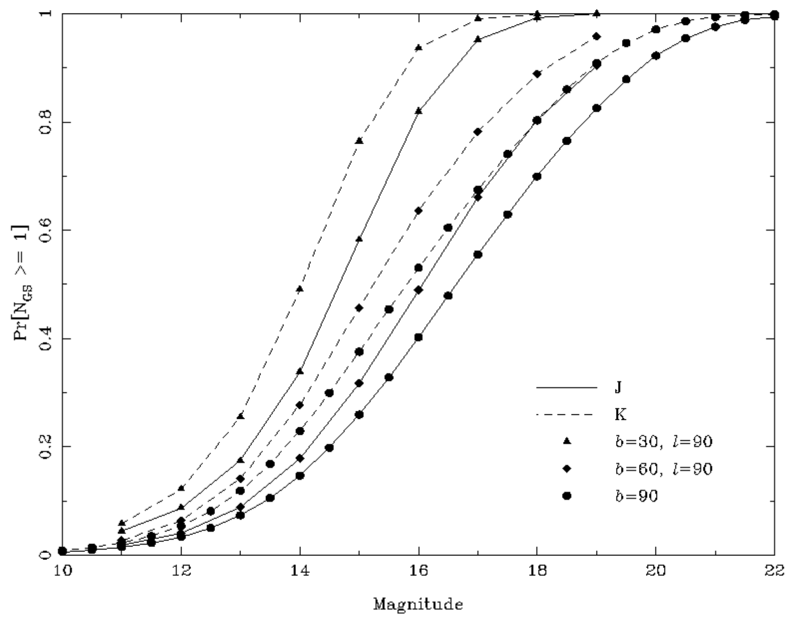

Figure 24: Guide star acquisition probabilities at *J* (*solid* lines) and *K* (*dashed lines*) for Galactic latitudes of 30º (*triangles*), 60º (*diamonds*), and 90º (*circles*).

3.5.3 Guide Star Selection

Selection of specific guide stars requires detailed knowledge of stars in the vicinities of a science target. The USNO catalog is one of the largest star catalogs in existence. However, tests show that it is incomplete, at least in the vicinity of external galaxies that are prime GSAOI targets. Digitized Sky Survey images show faint stars, but only in clear sky regions away from other objects and where the original photographic plates were not saturated. The 2MASS near-infrared sky survey is good for identifying near-infrared OIWFS stars. However, the on-line version is currently only ~ 50% complete and, as with all ground-based surveys, its relatively coarse spatial sampling (~ 1″) limits its ability to reveal faint stars against extended objects. HST WFPC2 and NICMOS images, where available, provide the best data for selecting faint guide stars, especially near bright extended objects such as galaxies. In practice, a combination of all four images is required to confidently predict the subarcsecond structure of an object and select MCAO, OIWFS, and ODGW guide stars.

A Perl script (*gs_search.pl*) that was originally written for NIFS has been modified to automate this process for GSAOI. *gs_search.pl* obtains and displays second generation Digitized Sky Survey red images, 2MASS *K* band images, HST WFPC2 and NICMOS preview images, and overlays USNO catalog stars. A file containing a list of object names is input to *gs_search.pl*. The script then uses the name resolver function of the NASA Extragalactic Database (NED) to obtain object coordinates, retrieve the various images from on-line sources, and displays them along with overlays of USNO catalog stars and the GSAOI imager field on a workstation screen. The display can be recentered at any position in the field, rotated to a convenient position angle, object coordinates and magnitudes can be printed, and suitable guide stars can be identified. This tool has been used to assess guide star availability for each of the science drivers addressed in §2.

Near-infrared imaging observations are dithered to permit accurate sky measurement. The dither offsets can be small when the science targets are point sources. In this case, the same guide stars can be used for each dither position as long as they remain within the peripheral OIWFS fields. Larger dither offsets are required for extended science targets because the offset must be at least as large as the object. Different guide stars are often then required for each dither offset. This places additional constraints on the availability of suitable guide stars.

4 References

Arnold, R., & Gilmore, G. 1992, MNRAS, 257, 225
Baraffe, I., Chabrier, G., Allard, F., & Hauschildt, P. H. 2002, A&A, 382, 563
Brandl, B., Brandner, W., Eisenhauer, F., Moffat, A. F. J., Palla, F., & Zinnecker, H. 1999, A&A, 352, L69
Close, L. M., & McCarthy, D. W. 1994, PASP, 106, 77
Côté, P., Welch, D. L., Fischer, P., & Irwin, M. J. 1993, ApJ, 406, L59
Dayal, A., Latter, W. B., Beiging, J. H., Meakin, C., Kelly, D. M., Hora, J. L., & Tielens, A. G. G. M. 2000, in Asymmetrical Planetary Nebulae II: From Origins to Microstructures, eds. J. H. Kasner, N. Soker, & S. Rappaport, ASP Conf. Ser., 199, 221
Freedman, W., et al. 2001, ApJ, 553, 47
Ibata, R. A., Gilmore, G., & Irwin, M. J. 1994, Nature, 370, 194
Jenkins, C. 1996, "Optimal pixel sizes in the OIWFS", Gemini internal document
Jensen, J. B., Tonry, J. L., Thompson, R. I., Ajhar, E. A., Lauer, T. R., Rieke, M. J., Postman, M., & Liu, M. C. 2001, ApJ, 550, 503
Kalirai, J. S., Ventura, P., Richer, H., Fahlman, G. G., Durrell, P. R., D'Antona, F., & Marconi, G. 2001, AJ, 122, 3239
Lucas, P. W., Roche. P. F., Allard, F., & Hauschildt, P. H. 2001, MNRAS, 326, 695
Lynden-Bell, D. 1976, MNRAS, 174, 695
Lynden-Bell, D., Faber, S. M., Burstein, D., Davies, R. L., Dressler, A., Terlevich, R. J., & Wegner, G. 1988, ApJ, 326, 19
Lynden-Bell, D., & Lynden-Bell, R. M. 1995, MNRAS, 275, 429
McCaughrean, M. J. 1988, Ph.D. thesis, University of Edinburgh
Maihara, T., Iwamuro, F., Yamashita, T., Hall, D. N. B., Cowie, L. L., Tokunaga, A. T., & Pickles, A. 1993, PASP, 105, 940
Majewski, S. R., Munn, J. A., & Hawley, S. L. 1994, ApJ, 427,L37
Oliva, E., & Origlia, L. 1992, A&A, 254, 466
Persson, S. E., Murphy, D. C., Krzeminski, W., Roth, M., & Rieke, M. J. 1998, AJ, 116, 2475
Racine, R., Walker, G. A. H., Nadeau, D., Doyon, R., & Marois, C. 1999, PASP, 111, 587
Roddier, C., & Roddier, F. 1993, JOSA, 10, 2277
Roddier, C., Roddier, F., Stockton, A., Pickles, A., & Roddier, N. 1990, SPIE, 1236, 756
Schroeder, D. 1987, Astronomical Optics, p. 182
Searle, L., & Zinn, R. 1978, ApJ, 225, 357
Sobolev, V. G. 1978, Planet. Space Sci., 26, 703
Soria R., et al. 1996, ApJ, 465, 79
Tinney, C. G., Da Costa, G. S., & Zinnecker, H. 1997, MNRAS, 285, 111
Tinney, C. G. 1999, MNRAS, 303, 565
Tonry, J. L., Blakeslee, J. P., Ajhar, E. A., & Dressler, A. 2000, ApJ, 530, 625
van den Bergh, S. 1993, AJ, 107, 971
Vassiliadis, E., Dopita, M. A., Meatheringham, S. J., Bohlin, R. C., Ford, H. C., Harrington, J. P., Wood, P. R., Stecher, T. P., & Maran, S. P. 1998, ApJ, 503, 253
Welch, C. A., Frank, A., Pipher, J. L., Forrest, W. J., & Woodward, C. E. 1999, ApJ, 522, L69
Wood, P. R., Bessell, M. S., & Fox, M. W. 1983, ApJ, 272, 99
Zinn, R. 1993, in The Globular Clusters- Galaxy Connection, ed. G. H. Smith & J. P. Brodie, ASP Conf. Ser., 48, 38

This page is left blank intentionally.